ISSN 0915-6348

NATIONAL INSTITUTE FOR FUSION SCIENCE

SOKENDAI Lecture Series "Mathematics for Physics" Selected Topics on Nonlocal Analysis of Plasma Waves and WKB Method (Lecture Series-II)

Heiji Sanuki

(Received - Mar. 16, 2007)

NIFS-PROC-66

Apr. 2007

RESEARCH REPORT
NIFS-PROC Series

TOKI, JAPAN

SOKENDAI Lecture Series " Mathematics for Physics"

Selected Topics on Nonlocal Analysis of Plasma Waves and WKB Method

(Lecture Series-II)

Heiji Sanuki

National Institute for Fusion Science and Graduate University for Advanced Studies, Toki 509-5292,Japan

Abstract

In this series of lectures, an attempt giving an introductory presentation of a variety of complementary methods and viewpoints that may be used in the study of broad spectrum of linear and nonlinear phenomena is presented. The organization of this series of lectures consists of the three perspectives such as (1) mathematical tools of nonlinear phenomena, (2) plasma wave analyses, WKB Method and related Topics in inhomogeneous plasmas, and (3) topics associated with the bifurcation phenomena in plasmas.

Second, selected topics on nonlocal analyses of plasma wave and WKB (Wentzel- Kramers- Brillouin) method in inhomogeneous plasmas are presented in this article (Lecture Series-II).

Keyword: Linear plasma waves(electrostatic and electromagnetic modes), local and nonlocal dispersion relations, nonlocal stability analyses, integral equation in K-space, WKB methods, direct numerical integration method, saddle point method of integration,asymptotic behavior near turning points, temperature gradient instabilities(sheared slab and toroidal ITG, ETG, SWITG and SWETG)

The topics of the present lecture have been prepared and presented partly for the discussion meetings for following research tasks:

1)Heiji Sanuki, “ 不均一プラズマ中の波動解析への WKB 法の応用 “
「複素ＷＫＢ法の理論と物理学への応用」に関する京都大学数理解析研究所講究録７８８、１９９２年６月,pp59-75. Kyoto University, Research Institute for Mathematical Sciences (RIMS),
2)Heiji Sanuki,“プラズマ波動の非局所解析と WKB 法”、 京大数理解析研究所共同利用研究（平成１４年度, 2003) organized by T. Kawai,
研究計画題目：「高階 Painleve 方程式の Stokes 図形の西川現象」
(2003, March 7, 8 RIMS, Kyoto University)

Contents

1. Introduction
2. Stability Analysis based on “Local Dispersion Relation”
3. Eigenmode Analysis based on Differential Equation
   3.1 WKB solusion
   3.2 Matching of quasi-classical functions
   3.3 Quantization condition
4. Eigenmode Analysis based on Integral Equation in K-Space
   4-1. Integral equation for electrostatic and electromagnetic modes
   4-2.WKB method
      4-2-1.Eikonal functions in k-space and solution of integral equation (electrostatic modes)
      4-2-2. Asymptotic behaviors near turning points
      4-2-3. Stability analysis of electrostatic waves for weakly dissipative cases

4-2-4. Eikonal function in k-space and solution of integral equation (electromagnetic modes)
4-3. Direct numerical integration method
4-4. Extension of ray tracing theory for inhomogeneous plasmas based on eikonal function formula
5. Examples of Nonlocal Stability Analysis based on Integral Equation in K-space and related Transport
5-1. Example of WKB-type eigenmode analysis
5-2. Example of eigenmode analysis based on representation in an orthogonal basis sets
5-3. Comparison between experimental observations and theoretical results (Bumpy torus and mirror devices)
5-4. Nonlocal ITG and ETG modes based on electrostatic, low beta, and full beta models
5-5. Algebraic formula for critical gradient associated with anomalous transport
6. Acknowledgements
7. References
8. Appendices
(A-1) One-dimensional WKB problem(in general)
(A-2) Quantization and energy level for Coulomb Potential
(A-3) Physical meaning of the eikonal function g (k)
(A-4) Multi-valued functions

1. Introduction

An enormous number of particles and lots of modes are contained in plasma systems. Mathematical models are often discussed based on assumptions and simplifications. Considerations from these models have formed the basis for the study of plasma waves involved in systems under consideration in this lecture.

These modes and models are characterized according to the following key features:

(1) Modes are the **electron modes** or **ion modes**, and also **electrostatic** or **electromagnetic modes**,
(2) Modes propagate in the **parallel** or **perpendicular** direction to the magnetic field,
(3) Modes are the **collisional** or **collisionless**,
(4) Magnetic field is uniform or nonuniform (**magnetic shear**),
(5) Electric field is homogeneous or inhomogeneous (**velocity shear**),
(6) Density or temperature, or both density and temperature are homogeneous or inhomogeneous (**density and/or temperature gradients**),
(7) Plasma is composed of **electrons** and **ions**, or together with **other components** such as impurities, trapped particles and energetic particles (ions or electrons),
(8) **Local** or **nonlocal**,
(9) **Linear** or **nonlinear**,
(10) Other features.

In addition, it is usually employed to restrict the range of parameters under consideration and also some assumptions are made in order for an approximate dispersion relation to be valid. In particularly, various analytical methods have been discussed to study the stability of microinstabilities in inhomogeneous plasmas. Typical these methods are the analyses to solve the local dispersion relation, eigenvalue problems based on differential equation and integral equation in real space or wave number space (k-space). To solve these problems, the WKB method and

numerical analyses such as shooting method for differential equations and direct numerical integration method for integral equation were investigated. Analytical methods based on the second order differential equation yield lots of information associated with stability characteristics and the WKB method based on differential equation in the configuration space is also well developed. It should be noted that this method is not applicable to the stability analysis in short wavelength regime because it is based on the assumption, $k\rho << 1$, where k is the wave number in the inhomogeneous direction and ρ is the Larmor radius. Then, the eigenvalue problems based on the integral equation should be solved to get more precise information of stability feature of the waves.

As mentioned above, the success in solving the integral equation has come from two approaches: WKB method [1-4] and direct integration methods [5-8]. In the WKB method, an eikonal form [9] is postulated for the eigenfunction, and the integral is done analytically by the method of steepest descent. The algebraic equation must then be solved numerically along with a quantization condition to determine the integration contour of the eikonal. In direct numerical integration, the integral equation is reduced to quadrature, turning the integral into a numerical matrix equation. The two methods are complementary in that they work best at opposite ends of the k-space spectrum. Eigenvalue analyses based on the integral equation in k-space have been extended into multi-species plasma [10], electromagnetic modes and drift waves in cylindrical plasmas [11]. This method is applicable to the stability analysis of highly localized modes in case of $k\rho \geq 1$. It should be noted that the analysis based on WKB method is restricted to the case of weakly unstable modes. Recently, intensive research attention is focused on understanding the anomalous transport in magnetically confined plasmas. Experimental evidence shows that this anomalous transport is governed by short wavelength mode turbulence. So, the drift waves such as the ion temperature gradient (ITG) mode and also electron temperature gradient (ETG) modes are actively studied with a gyrokinetic integral equation codes in sheared slab plasmas

[12-15].

In the next Chapter, the stability analysis based on the local dispersion relation is briefly surveyed. In the chapter 3, eigenmode analysis (WKB solution) based on 2nd order differential equation will be discussed. Eigenmodes analysis for both electrostatic and electromagnetic modes based on integral equation in k-space is introduced in Chapter 4. Both the WKB method and the direct numerical integration method will be discussed in this Chapter. Also, asymptotic behavior near turning points in k-space will be discussed. Chapter 5 will be devoted to examples of nonlocal stability analysis based on integral equation in k-space. The Concluding remarks will be presented in the last Chapter.

2. Stability Analysis based on "Local Dispersion Relation"

An assortment of plasma modes appears often in plasma textbooks. Modes are identified sometimes by the name of their discoverer or by a descriptive name, but more frequently they are identified by so called dispersion relation. Since a several of approximations are applied to obtain relatively simple dispersion relations for these modes, the mutual relationships between different modes are usually not straightforward. One of the elegant representations of these modes is so called "Clemmow-Mullaly-Allis Diagram (CMA-Diagram). In this diagram, a particular mode may be identified with an entire wave-normal surface, and the surface can be traced in the parameter space until it disappears due to the appearance of a **cutoff** or a **resonance**. (See, Ref.16) We have essentially two approaches, namely, fluid theory and a more refined treatment- kinetic theory. In general, the kinetic approach requires more mathematical calculations than the fluid one. In some plasma problems, neither fluid nor kinetic theory is sufficient to describe the complicated behavior of plasmas because we have to fall back on the tedious process of following the individual particle trajectories. Although it can solve only problems often in one or two dimensions, computer simulations may play an important role in these problems. Other lecturer will give the lecture

associated with this topic.

As an example, we here consider the dispersion relation in inhomogeneous plasmas. For simplicity, we employ the slab geometry with uniform magnetic field $B_0\hat{e}_z$, which is along the z-direction. Also, the density and temperature change only in the x-direction, namely, $(\nabla n)\hat{e}_x$, $(\nabla T)\hat{e}_x$, where $\hat{e}_x,\hat{e}_y,\hat{e}_z$ are the unit vector along x, y, z-directions, respectively. If we discuss the low-β collisionless plasma, and also neglect the magnetic compression effect ($A_\perp \cong 0$) and modes propagate in y-z plane ($\vec{k}=(0,k_y,k_z)$), the perturbed fields are given approximately under these conditions as

$$\vec{E} = -\nabla\phi - \frac{1}{c}\frac{\partial A}{\partial t}\hat{e}_z,\ \vec{B} = \nabla\times(A\hat{e}_z), \tag{2-1}$$

and we express the scalar and vector potentials in the following Fourier expansion form

$$\{\phi(\vec{r},t),A(\vec{r},t)\} = \{\bar{\phi}(x),\bar{A}(x)\}e^{i(\vec{k}\cdot\vec{r}-\omega t)}, \tag{2-2}$$

where $\vec{k}\cdot\vec{r} = k_y y + k_z z$. Substitution of (2-1) and (2-2) into Maxwell and Poisson equations yields the following relation (Ref.17)

$$\begin{pmatrix} k^2+Q-P & (\omega/k_z c)P \\ -(\omega/k_z c)P & k^2+(\omega/k_z c)^2 P \end{pmatrix}\begin{pmatrix}\bar{\phi}\\ \bar{A}\end{pmatrix} = 0. \tag{2-3}$$

From the determinant of (2-3), we have the following dispersion relation

$$P\left[\left(\frac{\omega}{k_z c}\right)^2 Q - k^2\right] + k^2 Q \cong 0, \tag{2-4}$$

where we neglected k^2 term compared with $Q-P$ term in the (1,1) metric component of (2-3) on the basis of the assumption, $k^2 << {k_d}^2$, in which ${k_d}^2 = (4\pi n_0 e^2/T)$ is the Debye wave number. The explicit forms for P and Q in (2-3) or (2-4) are defined as (see, Esq. (2.9b)-(2-10) in Ref.17))

$$P = \sum_{e,i} {k_d}^2\{(1+\frac{\tilde{\omega}_*}{\omega})e^{-b}I_0 W - \frac{\omega_*}{\omega}\eta(\frac{1}{2}-\varsigma^2 W)e^{-b}I_0\}, \tag{2-5}$$

$$Q = \sum_{e,i} {k_d}^2\{1-(1+\frac{\tilde{\omega}_*}{\omega})e^{-b}I_0 - \frac{\omega_*}{\omega}\frac{\eta}{2}e^{-b}I_0\}, \tag{2-6}$$

where ${v_T}^2 = (2T/m)$ is the thermal velocity, $b = {k_y}^2\rho^2/2$, $I_n(b)$ is the nth order modified Bessel function (n=0, 1, 2…). In (2-5) and (2-6), we define

the following notation,

$$W(\varsigma=\omega/|k_z|v_T)=\int_{-\infty}^{\infty}dv_z\frac{k_zv_z}{\omega-k_zv_z}F_z=-[1+\varsigma Z(\varsigma)], \qquad (2\text{-}7)$$

with the abbreviation of

$$Z(\varsigma)=\frac{1}{\sqrt{\pi}}\int dx\frac{\exp(-x^2)}{x-\varsigma}, \qquad (2\text{-}8)$$

which is the well-known dispersion function. We also used the notations

$$\tilde{\omega}_*=\omega_*[1-\frac{1}{2}\eta(1+\chi)],\ \chi=2b[1-\frac{I_1(b)}{I_0(b)}],\ \eta=\nabla\ln T/\nabla\ln n, \qquad (2\text{-}9)$$

and $F_z=(m/2T\pi)^{1/2}\exp[-(m/2T)v_z{}^2]$ in (2-7) is the z-component of the Maxwellian velocity distribution function and $\omega_*=(cT/qB)(\nabla n_0/n_0)k_y$ in (2-9) is the diamagnetic drift frequency. It should be noted that the dispersion relation (2-4) with (2-5) and (2-6) is the general form of **local dispersion relation in inhomogeneous plasmas** and it includes lots of modes such as the drift waves and temperature gradient modes. It should be noted that we have electrostatic modes in case of $\beta<<m_e/m_i$ and electromagnetic modes for $m_e/m_i<\beta<<1$. We note that plasma dispersion function $W(\varsigma)$ instead of $Z(\varsigma)$ is often used in Russian textbooks (see, (2-8) and (2-9)). Taking the electrostatic limit, $\overline{A}\to 0,\ \omega/k_zc\to 0$, the dispersion relation can be simplified to be a dispersion relation for electrostatic modes,

$$(k^2+Q-P)\phi(k)=0, \qquad (2\text{-}10)$$

and for $A_\perp\neq 0$, (2-2) becomes (3×3) metric equation

$$\begin{bmatrix}M_{11}&M_{12}&M_{13}\\M_{21}&M_{22}&M_{23}\\M_{31}&M_{32}&M_{33}\end{bmatrix}\begin{bmatrix}\overline{\phi}\\\overline{A}_\perp\\\overline{A}_{//}\end{bmatrix}=0. \qquad (2\text{-}11)$$

We finally obtain the dispersion relation from $\det(M_{ij})=0$.

3. Eigenvalue Analysis based on Differential Equation

For simplicity, we here consider the eigenvalue program for

electrostatic modes in inhomogeneous plasmas based on the differential equation. If a quasiclassical approximation is employed, we can express perturbed quantities as

$$\phi(\vec{r},t) = \bar{\phi}\exp[i(\int k_x(x')dx' + k_y y + k_z z - \omega t)], \qquad (3\text{-}1)$$

where x is the coordinate in the direction of inhomogeneity. The local dispersion relation in this case is given by

$$\varepsilon(k_x(x), k_y, k_z; \omega) = 0, \qquad (3\text{-}2)$$

from which we can determine the frequency ω as a function of $k_x(x)$, k_y and k_z. Although this type of dispersion relation may give us certain qualitative information, we cannot determine the frequency ω quantitatively because the spatial structure of $k_x(x)$ cannot be determined by the local dispersion relation. The standard treatment of eigenmode analysis in inhomogeneous plasmas is the following. We first replace $k_x(x)$ by $i\partial/\partial x$ in the local dispersion relation such as (3-2) and then expand it up to the second order with respect to $k\rho$ with $k\rho << 1$. We finally have the following second order differential equation

$$\frac{d^2\phi}{dx^2} - P(x, k_y, k_z; \omega)\phi(x) = 0. \qquad (3\text{-}3)$$

In the derivation of (3-3), we used some useful relations associated with the dispersion function $Z(\varsigma)$ and modified Bessel function $I_0(b)$ in the forms (Ref.18 and Ref.19).

1) Differential equation for $Z(\varsigma = x + iy)$:

$$\frac{dZ}{d\varsigma} = -2[1 + \varsigma Z], \quad \frac{d^2Z}{d\varsigma^2} + 2\varsigma\frac{dZ}{d\varsigma} + 2Z = 0, \quad Z(0) = i\sqrt{\pi}. \qquad (3\text{-}4)$$

2) Real argument (y=0):

$$Z(x) = e^{-x^2}[i\sqrt{\pi} - 2\int_0^x dt e^{t^2}]. \qquad (3\text{-}5)$$

3) Imaginary argument (x=0):

$$Z(iy) = i\sqrt{\pi}\exp(y^2)[1 - erf(y)]. \qquad (3\text{-}6)$$

4) Power series (small argument):

$$Z(\varsigma) = i\sqrt{\pi}\exp(-\varsigma^2) - 2\varsigma[1 - \frac{2}{3}\varsigma^2 + \frac{4}{15}\varsigma^4 + ...]. \quad (3\text{-}7)$$

5) Asymptotic series ($|\varsigma| >> 1$):

$$Z(\varsigma) = i\sqrt{\pi}\sigma\exp(-\varsigma^2) - \frac{1}{\varsigma}[1 + \frac{1}{2\varsigma^2} + \frac{3}{4\varsigma^4} + ...], \quad (3\text{-}8)$$

where $\sigma = 0$ ($y > 1/|x|$), 1 ($|y| < 1/|x|$), 2 ($-y > 1/|x|$).

For the terms including the modified Bessel Function, we have the following power series and asymptotic series formulae

6) $I_0(b)e^{-b} < 1$, (for all of b). (3-9)

7) $I_0(b)e^{-b} \cong 1 - b + ...$, (for b<<1). (3-10)

8) $I_0(b)e^{-b} \cong 1/\sqrt{2\pi b} + ...$, (for b>>1). (3-11)

We note that we used the power series expansion (3-10) in the derivation of (3-3). Since $k_x\rho << 1$ is assumed for the derivation of (3-3), this method becomes inappropriate for strongly localized modes with $k_x\rho \geq 1$. Eigenmode analysis applicable to the case with $k_x\rho \geq 1$ has been developed based on an integral equation instead of the differential equation, which will be discussed in the next Chapter.

The eigenfrequency ω is determined from the localization condition (well known quantization condition in quantum mechanics) for the solution of (3-3).

3.1 WKB solution

We here discuss the WKB analysis on the basis of the second order differential equation. For simplicity, we consider electrostatic modes in inhomogeneous plasma, which is described by

$$\frac{d^2\phi}{dz^2} - Q(z)\phi = 0, \quad (3\text{-}12)$$

where $\phi(z)$ is the electrostatic potential and $Q(z)$ is complex in general. We now define the two turning points of $\phi(z)$ in the complex plane, z_1 and z_2, where $Q(z_1) = Q(z_2) = 0$. If one define a curve C as $Q(z_c = x_c + iy_c)$ is real

along C, then $Q(z_c) < 0$ $(z_1 < z_c < z_2)$ and $Q(z_c) > 0$ $(z_c < z_1, z_c > z_2)$. We finally obtain the WKB solution as

$$\phi(z_c) = \sum_{+,-} A_{\pm} Q^{-1/2}(z_c) \exp[\pm \int_{z_1,z_2}^{z_c} Q^{1/2}(z) dz], \qquad (3\text{-}13)$$

where $A_{\pm}$ are constants and this solution is valid on z_c far from z_1, z_2. The derivation of this type of WKB solution for differential equation such as Schrödinger equation will be discussed in Appendix [1]. Eigenvalue relation can be derived from the connection formulae between the solutions of inside and outside of turning points, in other word, from the existence of the solution along z_c for which $\phi(z_c) \to 0$ as $z_c \to \infty$,

$$\int_{z_1}^{z_2} [-Q(z_c)]^{1/2} dz_c = \pi(n + 1/2), \ (n = 0,1,2,....). \qquad (3\text{-}14)$$

The relation (3-14) is called the Bohr-Sommerfeld quantization condition. Typical example of Stokes line, anti-Stokes line, branch cuts and corresponding eigenfunction are roughly illustrated in Fig. 1.

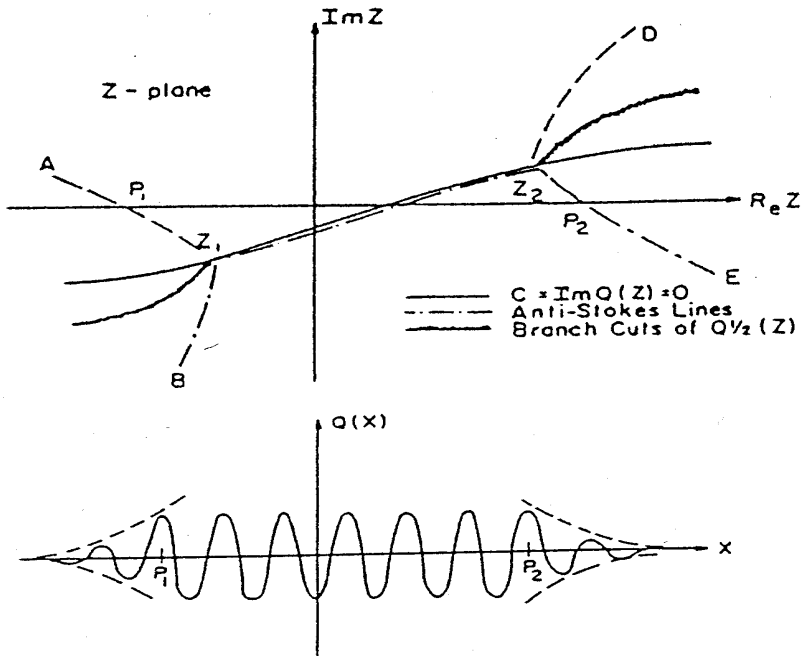

Fig. 1 Turning points, Stokes lines, anti-Stokes lines, branch cuts and corresponding eigenfunction are plotted(from[20]).

Questions

Two questions arise in connection with the applications at hand.

Q1: Can $\phi(z_c)$ be analytically continued to the x-axis to give desired solution $\phi(x)$?

Ans.: From (3-13), we see that the answer will be "Yes" provided we do not cross the branch cuts of the function $\sqrt{Q(z)}$ emanating from the two zeros in going from the curve C to the x-axis. This can be arranged by letting the branch cut from z_1, z_2 join at $z=\infty$ as shown in Fig. 1. Then, we can write approximately the solution along the x-axis as

$$\phi(x) = \sum_{+,-} A_{\pm} Q^{-1/2}(x) \exp[\pm \int_{z_1, z_2}^{x} Q^{1/2}(z) dz]. \qquad (3\text{-}15)$$

Q2: Does the solution $\phi(x)$ go to zero as $x \to \pm\infty$?

Ans.: To answer this question, we have to examine the exponential factor near two turning points(see,(3-18)). Assuming that Q has the only first-order zeros, near the turning point z_2, we expand Q (z)

$$Q(z) \approx (z - z_2)(\frac{\partial Q}{\partial z})_{z=z_2} \equiv (z - z_2) Q_{z2}, \qquad (3\text{-}16)$$

and the exponential becomes

$$\exp[\int_{z_2}^{z} (z - z_2)^{1/2} \sqrt{Q_{z2}} dz] = \exp[\frac{2}{3}(z - z_2)^{3/2} \sqrt{Q_{z2}}]. \qquad (3\text{-}17)$$

In order for the solution to be completely oscillatory, the relation (3-17) tends to

$$\mathrm{Re}[\frac{2}{3}(z - z_2)^{3/2} \sqrt{Q_{z2}}] = 0. \qquad (3\text{-}18)$$

If one introduce the following amplitude and phase variables through $(z - z_2) = \rho e^{i\vartheta}$, $2/3\sqrt{Q_{z2}} = \mathrm{Re}^{i\alpha}$, the relation (3-18) reduces to

$$\mathrm{Re}[R\rho^{3/2} e^{i(\alpha + \frac{3}{2}\vartheta)}] = 0 \text{ namely, } \alpha + \frac{3}{2}\vartheta = (n + \frac{1}{2})\pi, \ (n = 0,1,2.....). \qquad (3\text{-}19)$$

Therefore, near z_2, the exponential factors will be purely oscillatory along three lines separated by angles of $2\pi/3$. These lines are the so-called "anti-Stokes" lines, which are also illustrated in Fig. 1.

It should be noted that when we can not expand $Q(z)$ in the form of (3-15), namely, the expansion fails far from the turning point z_2; we must use the relation,

$$\mathrm{Re}[\int_{z_2}^{z}\sqrt{Q(z')}dz'] = 0, \qquad (3\text{-}19)$$

which determines the anti-Stokes lines. These lines are also defined for the turning point z_1 and since we know that the exponent is purely oscillatory along the curve C between z_1 and z_2, this portion of the curve must be an anti-Stokes lines for both turning points. The significance of the anti-Stokes lines lies in the fact that, for points in the z-plane other than ones on these lines, the exponential factors change from one to other when an anti-Stokes line is crossed. In other words, if a solution is exponentially decreasing in the region to the right of the line D, z_2, E, for instance, it will be exponentially increasing in the region above A, z_1, z_2 and D or in the region below B, z_1, z_2 and E. Since $\phi(z_c)$ is exponentially decreasing along C outside of z_1 and z_2, the analytically continued solution, $\phi(z)$, is also exponentially decreasing in the regions to the right of D, z_2, E, and to the left of A, z_1, B. Therefore, the answer to the second question is also "yes", that is $\phi(x)\to 0$ as $x\to\pm\infty$, if the relation (3-14) is satisfied, provided the x axis lies in these same regions as $|x|\to\infty$. This statement is equivalent to requirement that the anti-Stokes lines A z_1 and z_2E cross the x axis at some points P_1, P_2, respectively, as was shown in Fig.1. Examples how to derive the WKB solution and corresponding eigenvalue relation in some limiting cases have been studied in [20].

As for the mathematical discussions associated with the WKB solution for differential equations, in general, the structure near turning point is not always simple one in the case represented by (3-16). Extended theories for the WKB solution, which are applicable to more general cases with complicated potential structure, have been discussed by many authors [Refs. 9, 21,22,23,24 and 25]. In Ref. [9], N. Fröman discussed the double-well potential problem according to the general theory for higher

order approximations of the WKB type approach and derived the generalized quantization condition, which is not always same as (3-14). In order to check this situation, we study the quantization condition by considering the example of a one -dimensional square well with infinitely high walls. In this case, we have the following quantization condition [Ref.21]

$$\int_{x_1}^{x_2} k_n dx = k_n L = (n+1)\pi . \qquad (3\text{-}20)$$

The right hand side of (3-10) is different from $(n+1/2)\pi$. Here, L is the width of the well. Also, we see that when we consider the quantization condition for the **Coulomb radial wave functions** based on the **quasiclassical approximation**, the right hand side of the quantization condition reduces to (n+1) for $l=0$ and $(n+1/2)$ for $l\neq 0$. Detailed derivation will be discussed in Appendix II.

3.2 Matching of quasi-classical functions

We here discuss how to match the quasi-classical wave function in the acceptable region to the wave function in the evanescent region. As an example, we employ the wave potential shown in Fig.2, where the origin of coordinates corresponds to the point in which V (x)=E.

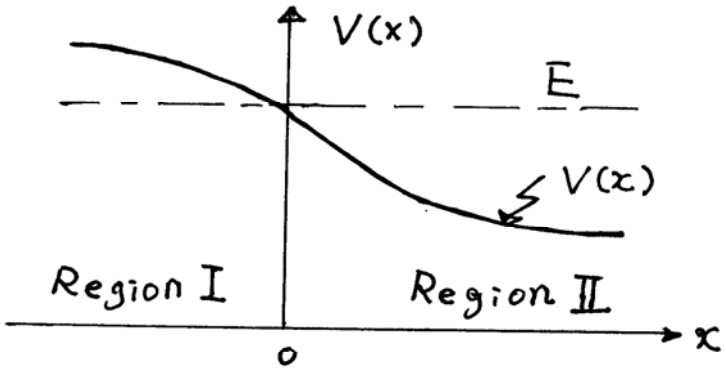

Fig.2 Wave potential profile is plotted. The region I (V (x)>E) is the evanescent region and the region II corresponds to the region accessible in the classical mechanism.

The quasi-classical solution in the region II in Fig.2 is given as from (A1-7) and (A1-8),

$$\varphi = \frac{a_1}{\sqrt{k}}\exp\left(i\int_0^x k dx\right) + \frac{a_2}{\sqrt{k}}\exp\left(-i\int_0^x k dx\right), \qquad (3\text{-}21)$$

while it is in the region I

$$\varphi = \frac{b_1}{\sqrt{|k|}}\exp\left(\int_x^0 |k| dx\right) + \frac{b_2}{\sqrt{|k|}}\exp\left(-\int_x^0 |k| dx\right). \qquad (3\text{-}22)$$

If the solution would be an analytic function of x around x=0, we have to continue the solution analytically from region II to region I to determine the relation between a_1, a_2 and b_1, b_2. It should be noted that we can not pass from region II to region I along the real axis since the quasi-classical approximation may break down in the neighborhood of x=0, in other word, as was mentioned in Appendix I, the condition $kl >> 1$ is not fulfilled because $k(0) \approx 0$ there. However, we will be able to overcome this difficulty by going around the point x=0 in the complex plane along an arc of large radius. To evaluate an appreciate radius of an arc in complex plane, we expand the potential V (x) around x=0, $V(x) \approx E + V'(0)x$. Then the momentum K (x) is given as $k(x) = \sqrt{-V'(0)x} = \alpha\sqrt{x}$, where $\alpha \approx \sqrt{V'(0)} \approx k_0/l$ with the abbreviations of $k_0 = \sqrt{2E}$ and l is the distance over which potential changes appreciably. Therefore, we finally obtain the following relation for the arc radius in order that the quasi-classical approximation should be applicable,

$$\frac{l}{(k_0 l)^{2/3}} << x_1 << l. \qquad (3\text{-}23)$$

Although we can find the matching condition around x=0 from the properties of the **Airy function**, which will be discussed later, we here derive these relations from a different approach instead of the method based on the Airy function.

We choose the radius ρ of the arc around the point x=0 of order of x_1, which is shown in Fig.3. By taking the potential to be linear with respect to x, we have approximately $k(x) = \alpha x^{1/2}$. Since in the complex plane we can put $x = \rho e^{i\varphi}$, we easily obtain the relation

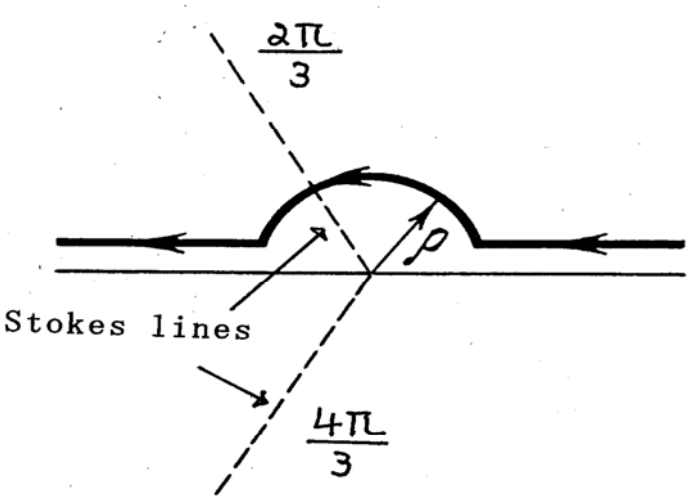

Fig.3 Integration path around x=0 point in complex plane

$$\frac{1}{\sqrt{k}}\exp\left[i\int_0^x k dx\right]=\frac{1}{\sqrt{\alpha\rho^{1/2}}}e^{-i\varphi/4}\exp[\frac{2}{3}\alpha\rho^{3/2}(i\cos\frac{3}{2}\varphi-sin\frac{3}{2}\varphi)]. \qquad (3\text{-}24)$$

As we go around the circle of radius ρ in the upper plane as shown in Fig. 3, the expression $e^{i(2/3)\alpha x^{3/2}}$ goes over firstly into s decreasing exponential and then, after crossing the line $\varphi=2\pi/3$, which is shown by dotted line in Fig. 3, into an increasing one. As soon as the increasing exponential appears, an exponential small error may come due to the inexactness nature of the quasi-classical approximation. It should be noted that the analytic continuation procedure gives us only the coefficient of the increasing exponent. Consequently we get

$$\frac{1}{\sqrt{k}}\exp[i(\int_0^x k dx-\frac{\pi}{4})]\rightarrow\frac{1}{i\sqrt{|k|}}\exp[\int_x^0|k|dx], \qquad (3\text{-}25)$$

where we lost a term, which is exponentially small compared with the right-hand side of (3-25). If we go around the point x=0 in the lower half plane, the solution (3-25) goes over firstly into an increasing exponential, and then goes into a decreasing one after crossing the line $\varphi=-2\pi/3$. The exponentially small correction lost in the region $-2\pi/3<\varphi<0$ due to

quasi-classical approximation goes over into an exponentially large term, after cross into the region $-\pi < \varphi < -2\pi/3$.

Suppose that there is only a decreasing exponential in the region (V>E), namely,

$$\Psi = \frac{1}{\sqrt{|k|}} \exp[-\int_x^0 |k| dx]. \qquad (3\text{-}26)$$

On the other hand, the solution for V<E is given as

$$\Psi = \frac{C_1}{\sqrt{k}} \exp[i\int_0^x k dx - i\varphi_1] + \frac{C_2}{\sqrt{k}} \exp[-i\int_0^x k dx + i\varphi_2]. \qquad (3\text{-}27)$$

We are now in the position to find the coefficients C_1, C_2 and the phase factors φ_1, φ_2 in (3-27). To derive those constants, we have to continue the decreasing solution (3-26) into the region with x>0. The analytical continuation of (3-26) in the upper half-plane yields

$$\Psi = \frac{1}{\sqrt{|k|}} \exp[-\int_x^0 |k| dx]$$

$$\rightarrow \quad \frac{1}{\sqrt{k}} \exp[-i\int_0^x k dx + i\frac{\pi}{4}] = \frac{e^{i\pi/4}}{\sqrt{\alpha\rho^{1/2} e^{i\varphi/4}}} \exp[\frac{2}{3}\alpha\rho^{3/2}(sin\frac{3}{2}\varphi - i\cos\frac{3}{2}\varphi)]. \qquad (3\text{-}28)$$

For $\varphi = 0$, we get the second term in (3-27) with $\varphi_2 = \pi/4, C_2 = 1$. Also, the analytical continuation of (3-26) in the lower half-plane gives

$$\frac{1}{\sqrt{k}} \exp[i\int_0^x k dx - i\frac{\pi}{4}] = \frac{e^{-i\pi/4}}{\sqrt{\alpha\rho^{1/2} e^{i\varphi/4}}} \exp[\frac{2}{3}\alpha\rho^{3/2}(-sin\frac{3}{2}\varphi + i\cos\frac{3}{2}\varphi)]. \qquad (3\text{-}29)$$

Comparison between (3-27) and (3-29) gives the relation $\varphi_1 = \pi/4, C_1 = 1$. The detailed derivation of the connection formula between region I and region II as shown in Fig.2, was discussed by Bohm [28] and Schiff [29].

When we carry out the analytical continuation of the solution (3-26) in the region I into the one in region II (see.Fig.2), we finally obtain the formula

$$\frac{1}{\sqrt{|k|}} \exp[-\int_x^0 |k| dx] \rightarrow \frac{2}{\sqrt{k}} \cos\left(\int_0^x k dx - \frac{\pi}{4}\right). \qquad (3\text{-}30)$$

Although the quasi-classical solution of the Schrödinger equation (A1-1) in the case of the potential as shown in Fig.2 is given by

$$\Psi \approx \frac{1}{\sqrt{|k(x)|}}\left(\int_0^x |k|dx\right)^{1/6} Ai[(-x/|x|)(3/2\int_0^x |k|dx)^{2/3}], \qquad (3\text{-}31)$$

where $Ai[z]$ are the Airy function and the asymptotic expansion form z>0 and z<0 are given as [23, 30]

$$A_i(z) \propto \frac{1}{2}\pi^{-1/2} z^{-1/4} \exp(-\frac{2}{3}z^{3/2}), \quad \text{for } z>0, \qquad (3\text{-}32)$$

$$A_i(z) \propto \pi^{-1/2}(-z)^{-1/4} \cos[\frac{2}{3}(-z)^{3/2} - \frac{\pi}{4}], \quad \text{for } z<0. \qquad (3\text{-}33)$$

The asymptotic behavior near turning point can be studied based on the formula (3-32) and (3-33) and will be discussed later.

For the potential profile as shown in Fig.2, from the properties of the Airy function such as (3-32) and (3-33), we get the following connection formula (right matching condition)(see, Ref. [29])

$$\frac{1}{\sqrt{k}}\exp[i\int_0^x kdx - i\pi/4] \rightarrow \frac{1}{i\sqrt{|k|}}\exp[\int_x^0 |k|dx] + \frac{1}{2\sqrt{|k|}}\exp[-\int_x^0 |k|dx], \qquad (3\text{-}34)$$

$$\frac{1}{\sqrt{k}}\exp[-i\int_0^x kdx + i\pi/4] \rightarrow \frac{-1}{i\sqrt{|k|}}\exp[\int_x^0 |k|dx] + \frac{1}{2\sqrt{|k|}}\exp[-\int_x^0 |k|dx]. \qquad (3\text{-}35)$$

From these relations (3-34) and (3-35), we easily obtain the relation (3-30).

3.3 Quantization condition

To derive the so called the quantization condition, we here consider the potential as shown in Fig.4.

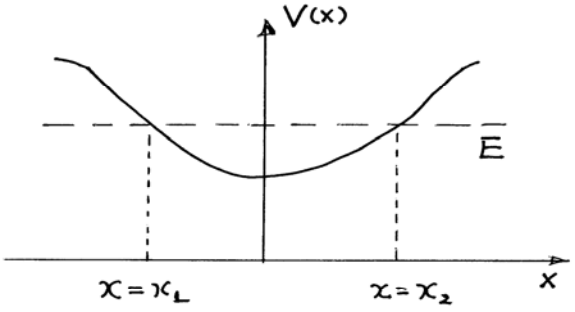

Fig.4 Potential profile V (x). Here, x_1 and x_2 are the turning points.

The quasi-classical solution of the Schrödinger equation can be written by matching the oscillating solutions to the exponentially decreasing ones at x_1 and x_2. The requirement that the two solutions should be identical yields the quantization condition.

These two solutions are given as

$$\psi_1 = \frac{a_1}{\sqrt{k}}\cos\left(\int_{x_1}^{x} k dx - C_1\pi\right), \quad \psi_2 = \frac{a_2}{\sqrt{k}}\cos\left(\int_{x}^{x_2} k dx - C_2\pi\right), \qquad (3\text{-}36)$$

where $C_1\pi\,(C_2\pi)$ is the phase resulting from matching to the decreasing exponential for $x < x_1\,(x > x_2)$, respectively. It should be noted that $C_1 = 1/4,\ C_2 = 1/4$ in cases where the potential has a linear dependence near the turning points, $x = x_1, x = x_2$. Finally, the requirement that the two solutions should agree, gives the following quantization condition

$$\int_{x_1}^{x_2} k dx = (n + C_1 + C_2)\pi \ . \qquad (3\text{-}37)$$

In the case where the potential has a linear dependence near the turning points, $x = x_1, x = x_2$ as mentioned above, (3-37) reduces to the well known quantization condition (3-14).

4. Eigenmode Analysis based on Integral Equation in K-Space

Since the effect of resonant wave-particle interaction and finite Lamor radius effect play an important role in plasmas, an eigenmode analysis including these effects in an inhomogeneous plasma is particularly important for studying stability, transport, heating of magnetically confined plasmas. As mentioned in the introduction, the conventional eigenmode analysis based on second order differential equation is applicable only to the case $k\rho << 1$, whereas a systematic method for eigenmode analysis of electrostatic waves has been developed based on an integral equation in the wavenumber space (k-space). This method has an advantage where it can treat the case $k\rho \geq 1$. When the plasma beta value becomes large, microscopic low frequency modes are accompanied by magnetic perturbations. However, an analysis for electromagnetic waves is

substantially difficult than that for electrostatic waves, since the former requires solutions of coupled and/or vector equations, whereas the latter needs only a scalar equation for electrostatic waves.

There are two key problems in the eigenmode analysis based on an integral equation: (1) derivation of integral kernel, (2) development of numerical scheme to get the eigenfrequency. As for the derivation of integral kernel, an efficient method to obtain the integral kernel has been discussed for the case of a Gaussian density profile in a uniform magnetic field. [1,2] although it is not so easy to obtain the integral kernel for a general density profile. For the modes with low radial mode number, the **direct integration method** gives the eigenfunction and eigenfrequency without requiring much computer time. For the modes with high radial mode number, the direct integration method requires an enormous computer time and memory because a fine spatial structure of eigenfunction may appear. In this case, we can apply a WKB approximation to the mode analysis. Although we discussed the so-called Bohr-Sommerfeld quantization condition, (3-14) and (3-37) for the second-order differential equation, a similar form of the quantization condition has been derived based on the integral equation method, which will be discussed later in this lecture. A generalized quantization condition valid for the electromagnetic case is also discussed by Berk and Pfirsch [31] and Watanabe et al. [32]. In [31], the WKB approximation based on an integral equation in the real space has been discussed. As mentioned in Sec.3.2, the WKB approximation is invalid near turning points. Therefore, Berk and Pfirsch rewrote the original integration equation in the k-space and derived a quantization condition in the form

$$\oint [k(x) + \delta k(x)]dx = (2n+1)\pi, \qquad (4\text{-}1)$$

where $\delta k(x)$ denotes the electromagnetic correction which is absent in the electrostatic case. However, the practical method to obtain eigenfrequencies on the basis of (4-1) has not been discussed in [31]. A systematic numerical scheme to calculate the eigenfrequency from the generalized quantization condition in the electromagnetic case is

discussed in [32], which will be introduced briefly later.

4.1 Integral equation for electrostatic modes and electromagnetic modes

We here discuss an eigenmode analysis for electrostatic modes with $k\rho \geq 1$ in inhomogeneous plasma. The analysis is based on an integral equation instead of a differential equation. Expressing a perturbed potential in the following Fourier integration form,

$$\phi(\vec{r},t) = \int_{-\infty}^{\infty} dk\phi(k)\exp(ikx + ik_{\perp}y + ik_{//}z - i\omega t), \qquad (4\text{-}2)$$

we can obtain the following integral equation for $\phi(k)$ as

$$F(k)\phi(k) = \int_{-\infty}^{\infty} K(k,k')\phi(k')dk', \qquad (4\text{-}3)$$

where $F(k) = k^2 + k_{\perp}{}^2 + k_{//}{}^2$ and we suppress the subscript x attached to the variables k_x and $k_x{}'$, which are the wave numbers in the direction of in homogeneity (x). It should be noted that the kernel $K(k,k')$ in (4-3) depends not only on k_x and $k_x{}'$ but also on $k_{\perp}, k_{//}$ and ω, although they are not explicitly written in the expression of $K(k,k')$. The integral equation for drift waves in the plasma including hot electron component together with the bulk components was derived in [10]. The integral equation for the Drift Cyclotron Loss Cone (DCLC) mode in slab geometry was also discussed [33]. By assuming low-beta electrostatic plasma in a straight magnetic field with a Gaussian density profile, an analysis of drift wave, drift cyclotron (DC) waves and drift cyclotron loss cone (DCLC) waves have been discussed in cylindrical geometry [11]. In the reference [11], we take the magnetic field to be uniform in space and directed along the x-axis. Also, the equilibrium distribution function for each species is chosen to be uniform in z and cylindrical symmetric, with a density profile which is Gaussian in r, the radial coordinate. Using a simplification associated with a decomposition of the potential into azimuthal eigenmodes with the definition

$$\Psi_m(k') = \frac{1}{\sqrt{2\pi}} \int_0^{2\pi} d\alpha' \Psi(\vec{k}_{\perp}{}')e^{-in\alpha'}. \qquad (4\text{-}4)$$

The final equation is an integral equation in $k = \left|\vec{k}_{\perp}\right|$ for a single azumuthal eigenmode of the perturbed potential

$$(k^2 + k_{//}{}^2)\Psi_m(k) = \int_0^{\infty} dk' k' \Psi_m(k') K(k,k'), \tag{4-5}$$

with the abbreviation of

$$K(k,k') = -\sum_j k_{Dj}{}^2 R^2 \exp\left(\frac{-(k^2 + k'^2)R^2}{2}\right) \sum_l I_l(kk'R^2\varepsilon) I_{l+m}(kk'R^2[1-\varepsilon]) B_l, \tag{4-6}$$

where

$$B_l = \frac{T_{\perp}}{T_{//}} + \left(\frac{T_{\perp}}{T_{//}} + \frac{l(1+\gamma^2) + m\gamma^2}{\varpi - l}\right)\varsigma_l Z(\varsigma_l). \tag{4-7}$$

Here, Z is the plasma dispersion function (2-8), I is the modified Bessel function as mentioned in Sec. 2, and $T_{\perp}(T_{//})$ the perpendicular (parallel) temperature component, $\gamma_j{}^2 = \rho_j{}^2 / L_j{}^2$, $R_j{}^2 = L_j{}^2 + \rho_j{}^2$ (ρ_j, L_j are the the Larmor radius and the guiding center scale length, respectively), and R_j is the density scale length in the present cylindrical coordinate system. The explicit expressions for other notations involved in (4-6) and (4-7) are represented in [10].

We next consider an integral equation in the k-space for electromagnetic modes in the nonuniform and magnetized plasma. For simplicity, the zeroth-order velocity space distribution function is assumed to be anisotropic Maxwellian with Gaussian density distribution. After the lengthy calculations, we obtain the following linear integral equation in k-space for the electromagnetic waves

$$\left(\frac{c^2}{\omega^2}\vec{k}\vec{k} - \vec{\vec{I}}\right)\vec{E}(k) - \frac{c^2}{\omega^2}\vec{k}(\vec{k}\cdot\vec{E}(k))$$
$$= \sum_j \frac{L_j}{\sqrt{2\pi}} \int_{-\infty}^{\infty} dk' \exp\left(-\frac{(k'-k)^2 L_j{}^2}{2}\right)\left[\vec{\vec{K}}(k,k') + \left(1 - \frac{T_{\perp j}}{T_{// j}}\right)\frac{\omega_{pj}{}^2}{2\omega^2}\sum_n G_j'(\varsigma_n)\vec{\vec{M}}_j(k,k')\right]\vec{E}(k'), \tag{4-8}$$

where $\vec{\vec{I}}$ is the unit tensor, $\vec{\vec{K}}(k,k')$ and $\vec{\vec{M}}(k,k')$ are the 3×3 metric tensor, and $\vec{E}$ is the vector representation of electric field. If we apply the following relations,

$$\vec{E}(\vec{r},t) = -\nabla\phi(\vec{r},t),\ (k^2 + k_\perp{}^2 + k_{//}{}^2)\phi(k) = \frac{4\pi}{i\omega}\vec{k}\cdot\vec{\sigma}(\vec{k},k',\omega)\cdot\vec{k}'\phi(k'), \qquad (4\text{-}9)$$

the linear integral equation (4-8) for the electromagnetic modes can be transformed into that of electrostatic modes [34]

$$(k^2 + k_\perp{}^2 + k_{//}{}^2)\phi(k) = -\sum_j \frac{L_j}{\sqrt{2\pi}}\int_{-\infty}^{\infty} dk' \exp\left(-\frac{(k'-k)^2 L_j{}^2}{2}\right)\frac{\omega_{pj}{}^2}{v_{T\perp}{}^2}$$

$$\times[1 + \frac{\omega + i\omega_j{}^*}{\sqrt{2}k_{//}v_{T//}}\sum_n G(\varsigma_n)I_n(b_j) + \frac{1}{2}\left(1 - \frac{T_\perp}{T_{//}}\right)\sum_n G'(\varsigma_n)I_n(b_j)]\phi(k'). \quad (4\text{-}10)$$

When we consider an isotopic temperature case, namely, $T_\perp = T_{//}$, the integral equation (4-10) reduces to the integral equation foe the electrostatic modes (4-3), which has been discussed in [1,2]. Also, it should be noted that the equation (4-8) could be transformed into the homogeneous local dispersion relation for the electromagnetic modes, when the condition $L \to 0$ is satisfied. The notation $G(\varsigma_n)$ and/or $G'(\varsigma_n)$ in (4-8) and/or (4-10) is defined by Eq. (26.a) in [34].

4-2 WKB method

We are now in the position how to solve the eigenvalue problem based on the integral equation, (4-3), (4-5) and (4-8). Here, we discuss a WKB method for an integral equation although the WKB approach has been already discussed in Sec.3.

4-2-1 Eikonal function in k-space and solution of integral equation (electrostatic modes)

We consider plasma with special inhomogeneity in the x-direction, and the inhomogeneous scale length κ^{-1} is of the order of L. Assuming that the typical wavelength k is in the range with $kL >> 1$; we can introduce an eikonal function f (x) in the case of differential equation such as (3-12) as

$$\phi(x) = \exp(-i\int^x f(x)dx), \qquad (4\text{-}11)$$

and one can determine f (x) in the form of an asymptotic series with respect

to $(kL)^{-1}$ and the eikonal function may give a " Bohr-Sommerfeld quantization condition" [9]. Also, we can introduce an eikonal function g (k) in the k-space for the integral equation (4-3) as

$$\phi(k) = \exp(-i\int^{k} g(k')dk'). \qquad (4\text{-}12)$$

It should be noted that the eikonal function could be determined after substituting it into the integral equation (4-3). The physical meaning of the eikonal function g (k) is discussed in Appendix 3.

Substitution of (4-12) into (4-3) yields the following integral equation

$$F(k) = \int_{-\infty}^{\infty} dk' K(k,k') \exp[-i\int_{k}^{k'} g(k'')dk'']. \qquad (4\text{-}13)$$

Here, we note that the integral equation (4-3) can be regarded as a three wave coupling equation among k, k' and κ, being of the order of L^{-1} where κ is a typical wave number of density inhomogeneity. Since a wave number matching condition, $k = k' + \kappa$ is to be satisfied in the three wave coupling process, the values of k' fall in the range $|k - k'| \le L^{-1}$, where we assumed the relation $|\kappa| \le L^{-1}$.

If the relations $kL >> 1$ and $|k - k'| \le L^{-1}$ are satisfied, the eikonal function $g(k'')$ in the integral of (4-13) can be expanded around k

$$g(k'') = g(k) + (k'' - k)g'(k) + O[L \cdot (kL)^{-2}] + \cdots \qquad (4\text{-}14)$$

where k indicates a position of the wave with wavenumber k, and g is of the order of L. Also, we use an asymptotic expansion of the eikonal function as

$$g(k) = g_0(k) + g_1(k) + \cdots, \qquad (4\text{-}15)$$

where $g_0(k), g_1(k), \cdots$ are determined to the order of $(kL)^{-1}, (kL)^{-2}$, and so on, respectively. Substituting (4-14) and (4-15) into (3-13) and using an asymptotic expansion with respect to $(kL)^{-1}$, we obtain

$$\exp[-i\int_{k}^{k'} g(k'')dk''] = \left[1 - i(k' - k)g_1(k) - \frac{1}{2}(k' - k)^2 \frac{dg_{0(k)}}{dk} + O[(kl)^{-2}]\right] \times \exp[-i(k' - k)g_0(k)]. \qquad (4\text{-}16)$$

From (4-13) and (4-16), we finally get the following relations

$$0 = H(k,g) = \int K(k,k')\exp[-i(k'-k)g_0(k)]dk' - F(k), \qquad (4\text{-}17)$$

$$g_1(k) = -\frac{i}{2}\left(\frac{\partial^2 H(k.g_0)}{\partial {g_0}^2}\right)\left(\frac{\partial H(k,g_0)}{\partial g_0}\right)^{-1}\frac{dg_0(k)}{dk}, \qquad (4\text{-}18)$$

with the abbreviations of

$$\frac{\partial H}{\partial g_0} = -i\int (k'-k)K(k,k')\exp[-i(k'-k)g_0(k)]dk, \qquad (4\text{-}19)$$

$$\frac{\partial^2 H}{\partial {g^2}_0} = -i\int (k'-k)^2 K(k,k')\exp[-i(k'-k)g_0(k)]dk. \qquad (4\text{-}20)$$

Equation (17) can be regarded as the Hamiltonian form in the (k, g)-space and determines the zeroth order eikonal function $g_0(k)$ and equation (4-18) gives the first order eikonal function $g_1(k)$. We can obtain the higher order terms of eikonal function in a similar way.

It should be noted that we could discuss a couple of different problems, depending on a profile of eikonal function in the g (k)-k plan. Typical three cases, namely, an elliptic function (Fig.5 (a)), hyperbolic functions (Fig.5 (b) and 5(c)) are briefly illustrated in Fig.5.

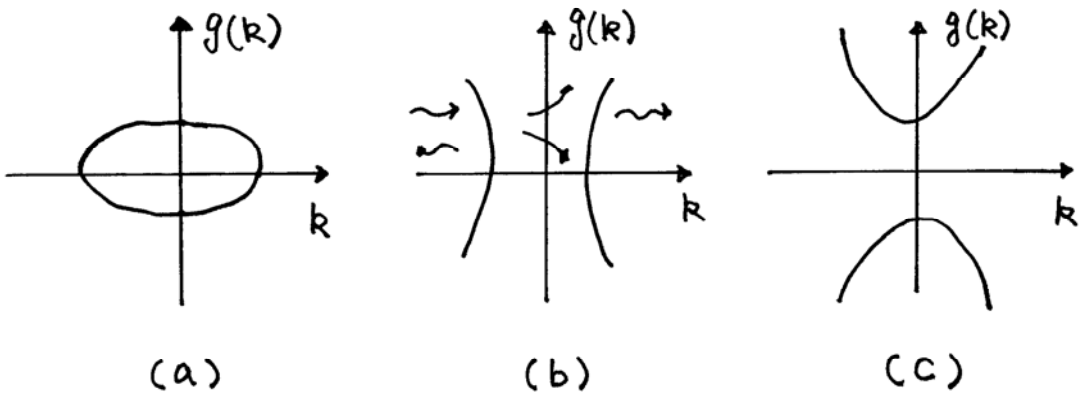

Fig.5 Typical three types of eikonal functions, namely Elliptic (a), hyperbolic (b) and (c) are illustrated.

Figures 5(a), 5(b) and 5(c) correspond to the cases associated with the

localized solutions, the reflection and/or penetration of waves, and mode conversion, respectively. These topics will be discussed in other lectures.

Using the eikonal function in the k-space, we next derive the quantization condition, which determines the eigenfrequency of the waves in inhomogeneous plasma. As we discussed in Sec.3, the eigenfrequency of the wave is determined from the condition for the existence of a spatially localized solution. Although we discussed the localized modes in the configuration (real) space in the previous session, we here restrict our discussion to localized modes in the k-space in the following analysis.

Derivation of quantization condition in the k-space

As discussed in Appendix 3, the eikonal function in the k-space g (k) denotes the x-coordinate of the wave with wave number k. From Eq. (4-17), we obtain the relation between $g_0(k)$ and k for fixed ω. In general, the curve g=g (k) for a localized mode becomes a closed loop in (k, g_0) plane. A typical case is illustrated in Fig.6.

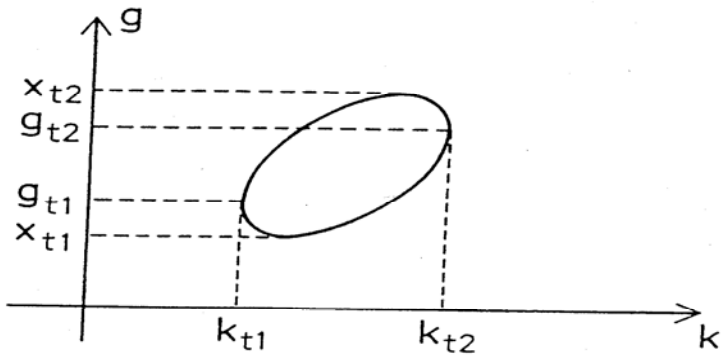

Fig.6 Schematic plot of g=g (k) curve for a spatially localized mode. Turning points in both configuration and k-space are also illustrated.

In Fig.6, $x_{t1}(x_{t2})$ is the turning point in x- coordinate and $k_{t1}(k_{t2})$ is the turning point in k space. In this case the solution of localized mode

can be constructed by the superposition of two independent plane waves with different k, in the range of $k_{t1} \le k \le k_{t2}$. We next investigate a behavior of the wave in the neighborhood of the turning points, where the expansion of the eikonal function (4-15) breaks down. Using the Hamiltonian (4-17), the turning points in the k-space are determined from the following relation

$$H(k_t, g_t) = 0 = \left[\partial H(k, g_0)/\partial g_0\right]_{k=k_t, g_0=g_t}. \tag{4-21}$$

We note that k_t and g_t are complex due to dissipation effects in plasmas. We here expand $H(k, g_0)$ around the turning point (k_t, g_t) as

$$H(k, g_0) \cong a(k - k_t) + b(g_0 - g_t)^2, \tag{4-22}$$

with

$$a \equiv [\partial H(k, g_0)/\partial k]_{k=k_t, g=g_t},\ b \equiv 1/2[\partial^2 H(k.g_0)/\partial {g_0}^2]_{k=k_t, g=g_t}, \tag{4-23}$$

where the relation (4-21) is used and higher order terms are neglected. From (4-17), (4-18), (4-21) and (4-22), we obtain the expressions for g_0 and g_1 as

$$g_0(k) = g_t \pm \left(-a/b\right)^{1/2}(k - k_t)^{1/2}, \tag{4-24}$$

$$g_1(k) = -\frac{i}{4}\frac{1}{k - k_t}. \tag{4-25}$$

We note that the zeroth and the first order terms of the eikonal function g (k) have a branch point and a pole at the turning point, respectively. To discuss problems associated with the branch point and the pole, we have to know the properties of a multivalued function such as (4-24). Mathematical basis for a multivalued function is briefly discussed in Appendix 4.

We introduce the branch cuts as shown in Fig.7 and construct a Riemann surface with two sheets in the k-space in order to make the eikonal function g (k) single-valued. Two independent solutions, $\psi_1(k)$ and $\psi_2(k)$, which correspond to the double values of $g_0(k)$ as shown in eq. (4-24), may be expressed as

$$\psi_{1,2}(k) = \exp\left[-i \int_{C_1, C_2} g(k) dk\right], \tag{4-26}$$

where C_1 and C_2 represent two independent paths of the integration from an arbitrary fixed point k_0 to k. The integration paths C_1 and C_2 are on the upper and on the lower Riemann surfaces, respectively.

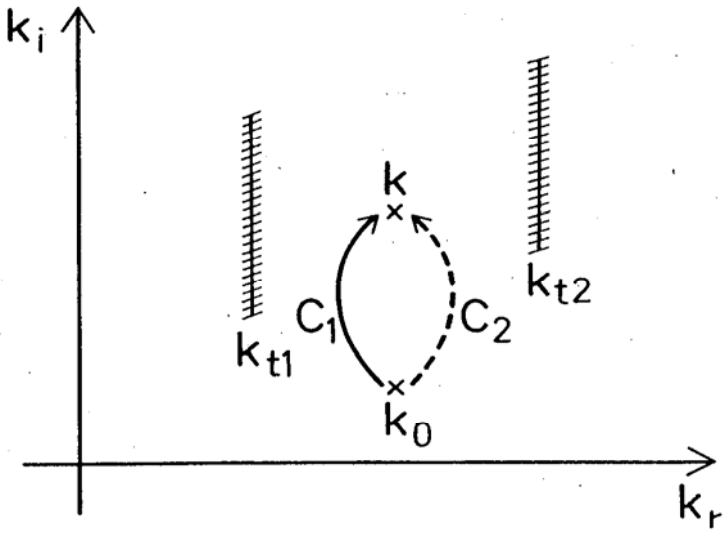

Fig. 7 Branch cuts in the k-space and two integration paths C_1 and C_2, which give two independent solutions $\psi_1(k)$ and $\psi_2(k)$. The shaded lines denote the branch cuts of eikonal function g (k), the solid curve represents the path in the upper Riemann surface and the dotted curve corresponds the path in the lower Riemann surface (from [1]).

Substitution of (4-15) with (4-24) and (4-25) into (4-16) and carrying out the integration with respect to k yields

$$\psi_{1,2}(k) \propto (k-k_t)^{-1/4} \exp\{-i[g_t(k-k_t) + \frac{2}{3}(-a/b)^{1/2}(k-k_t)^{3/2}]\}, \qquad (4\text{-}27)$$

where the sign of the term $(k-k_t)^{3/2}$ should be chosen appropriately depending on the location of k, that is either on the upper or lower Riemann surface. Also, some integration constant factor is omitted in (4-27). Although we discussed the anti-Stokes and Stokes lines of the differential equation (3-12) in the configuration space in the previous chapter, we here define both anti-Stokes and Stokes lines of (4-27) on the complex k-space in the following way: the Stokes lines from the relation

$$\mathrm{Re}\left[g_t(k-k_t) + \frac{2}{3}(-a/b)^{1/2}(k-k_t)^{3/2}\right] = 0, \qquad (4\text{-}28)$$

and the anti-Stokes lines from the relation

$$\mathrm{Im}\left[g_t(k-k_t)+\frac{2}{3}(-a/b)^{1/2}(k-k_t)^{3/2}=0\right]. \qquad (4\text{-}29)$$

In order to understand an asymptotic behavior of (4-28) and (4-20) for large k, we consider the following term in the exponential part of (4-27)

$$F(k)=-i\frac{2}{3}(-a/b)^{1/2}(k-k_t)^{3/2}\ . \qquad (4\text{-}30)$$

Introducing $k-k_t=re^{i\vartheta}$, (4-30) reduces to

$$F(k)=\frac{2}{3}(-a/b)^{1/2}r^{3/2}\exp[i\frac{1}{2}(3\vartheta-\pi)]. \qquad (4\text{-}31)$$

Then, **the relation defines the Stokes lines**

$$\frac{3}{2}\vartheta-\frac{\pi}{2}=n\pi, \qquad (4\text{-}32)$$

which gives $\vartheta=\pi/3(n=0),5\pi/3(n=2),3\pi(n=4)$ on the upper Riemann surface, where F is real and positive, and also $\vartheta=\pi(n=1),7\pi/3(n=3),11\pi/3(n=5)$ on the lower Riemann surface, where F is real and negative. Also, the **anti-Stokes lines** are defined by

$$\frac{3}{2}\vartheta-\frac{\pi}{2}=(n+\frac{1}{2})\pi, \qquad (4\text{-}33)$$

which gives $\vartheta=2\pi/3(n=0),2\pi(n=2),10\pi/3(n=4)$ on the upper Riemann surface and $\vartheta=4\pi/3(n=1),8\pi/3(n=3),4\pi(n=5)$ on the lower Riemann surface where F is real and purely imaginary.

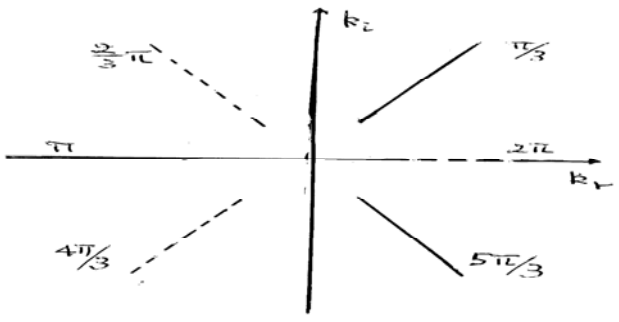

Fig. 8 Asymptotic behavior of Stokes (solid lines) and anti-Stokes (dotted lines) lines are briefly illustrated in complex k plane.

In order to study the fine structure of the Stokes and anti-Stokes lines around the turning point (left turning point) as shown in Fig. 7, we solve (4-28) and (4-29) numerically for the following parameters, $g_t = 1, a/b = -9/4$ and $k_t = 0$ as an example. The anti-Stokes and Stokes lines on the upper and lower Riemann surfaces are shown in Fig. 9 (a) and 9(b), respectively.

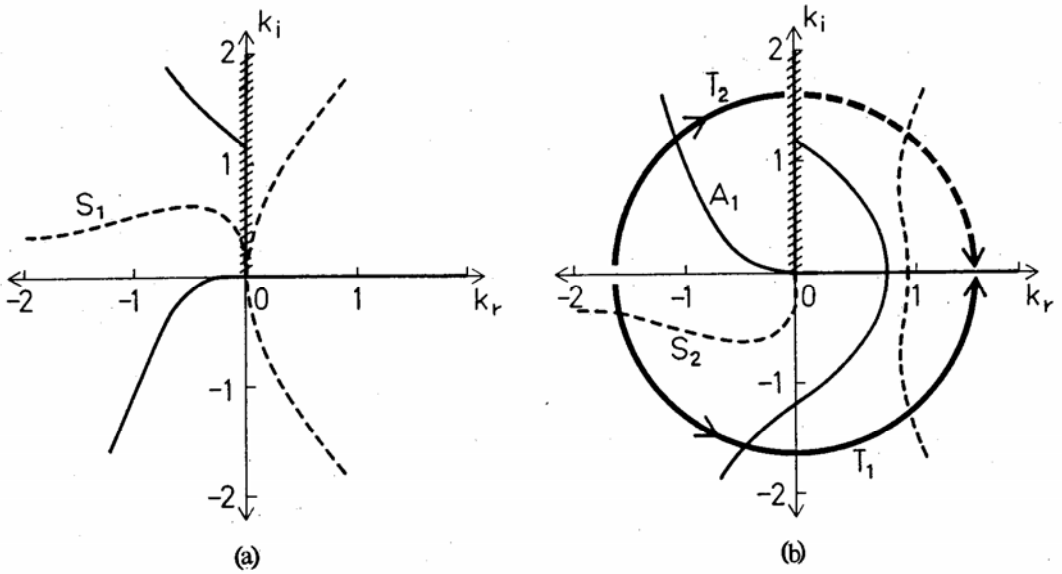

Fig. 9 Structure of upper (a) and lower (b) Riemann surfaces around the left turning point as shown in Fig. 7. The anti-Stokes lines are represented by solid lines and the Stokes lines are denoted by dotted lines. Also, the branch cut of eikonal function is illustrated by shaded solid line and path of analytical continuation is shown by thick solid line. (Ref. [1])

It turns out from Fig. 9 that the behavior of anti-Stokes and Stokes lines far away from the origin in Fig. 9 agree well with the asymptotic structure of Fig. 8. The solution $\psi_1(k)$ defined by (4-26) monotonically increases along the Stokes line S_1, which is shown in Fig. 9 (a), while the other independent solution $\psi_2(k)$ monotonically decreases along the Stokes line S_2 in Fig. 9 (b) as the point k moves away from the turning point. So, the localized solution $\psi(k)$ in the left hand region of the turning point k_{t1} is given as

$$\psi(k) = \exp\left[-i\int_{C_2} g(k)dk\right]. \qquad (4\text{-}34)$$

We connect the solution (4-34) into the one at the right hand region of the turning point k_{t1} and make an analytical continuation of the solution (4-34) along the path T_1 in Fig.9 (b). As was discussed in Sec.3.2, the solution (4-34) becomes an exponentially increasing function as the point k goes across the anti-Stokes line A_1, and we finally obtained the analytical continuation in the upper half plane in the following form

$$\psi(k) = \exp[-i\int_{C_3} g(k)dk] + \alpha\exp[-i\int_{C_4} g(k)dk], \qquad (4\text{-}35)$$

where the integration paths C_3 and C_4 are shown in Fig.10. The coefficient α cannot be determined from this analytical continuation along T_1 and it is determined by the analytical continuation in the lower half plane along T_2 in Fig.9 (b). We finally obtain $\alpha = 1$.

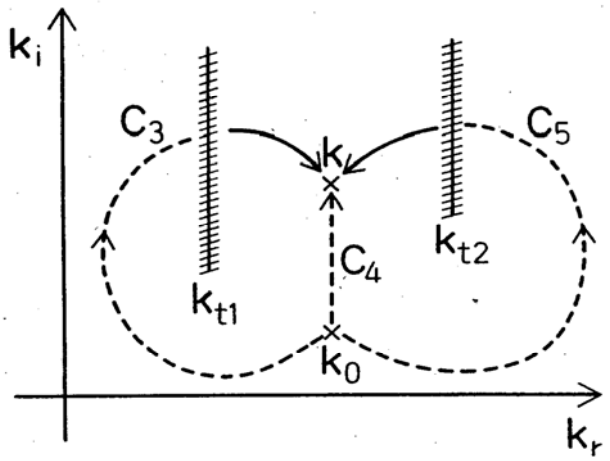

Fig.10 Integration paths, giving the localized solutions (4-35) and (4-36) in the region between k_{t1} and k_{t2}. (Ref. [1])

Similar argument can be done around the turning point k_{t2} as shown in Fig.7. Then, we find the following localized solution

$$\psi(k) = B\left\{\exp[-i\int_{C_4} g(k)dk] + \exp[-i\int_{C_5} g(k)dk]\right\}, \qquad (4\text{-}36)$$

where the integration paths C_4 and C_5 are shown in Fig.10. and B is some

constant. Since the solutions (4-35) and (4-36) should be identical, we finally have

$$B = 1, \tag{4-37}$$

$$1 = \exp[-i\int_{C_3} g(k)dk + i\int_{C_5} g(k)dk]. \tag{4-38}$$

It should be noted that the integrations along C_3 and C_5 in (4-38) could be replaced by a single integration along a single path Γ shown in Fig. 12.

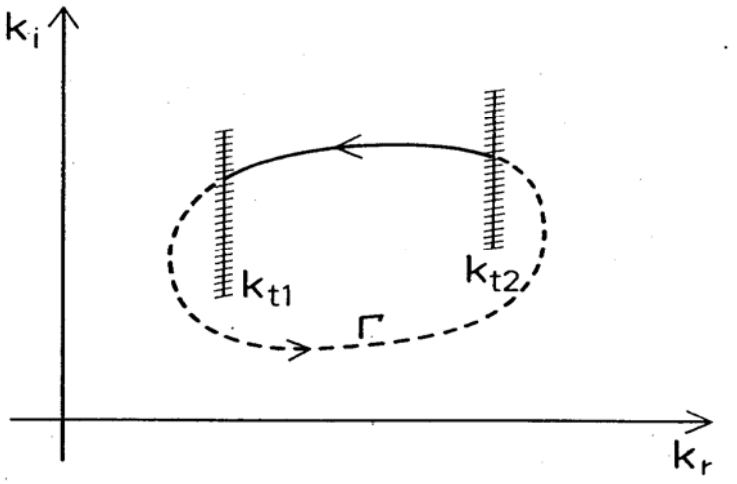

Fig. 11 Contour of integration path Γ to obtain the quantization condition. (Ref. [1])

The equation (4-38) yields the so-called "Quantization condition" which determines the eigenfrequency:

$$\int_{\Gamma} g(k)dk = 2(n+1)\pi, \quad (n = \pm 1, \pm 2, \cdots). \tag{4-39}$$

Substitution of (4-15) into (4-39) and carrying out the integration of $g_1(k)$ gives the quantization condition in the following form

$$\int_{\Gamma} g_0(k)dk = 2(n+\frac{1}{2})\pi, \quad (n = \pm 1, \pm 2, \cdots), \tag{4-40}$$

where we assumed that the function $g_1(k)$ has poles at the turning points but has no other singularities, so that we can deform the integration path Γ such that $g_1(k)$ can be approximated by the equation (4-25).

We finally discuss the derivation of quantization condition (4-40) on

the basis of a symbolic representation form. If we define the eikonal function $g_0(k)$ in both upper and lower Riemann surfaces,

$$g_{01} = g_t - (-a/b)^{1/2}(k-k_t)^{1/2} + g_1, \tag{4-41}$$

$$g_{01} = g_t + (-a/b)^{1/2}(k-k_t)^{1/2} + g_1. \tag{4-42}$$

The analytical continuation around the turning point k_{t1}, which is shown in Fig. 10, is represented by the following formulary

$$\psi(k) = \langle g_{01}|k_0,k\rangle - i\langle g_{01}|k_0,k_{t1}\rangle\langle g_{02}|k_{t1},k\rangle, \tag{4-43}$$

and the analytical continuation around the turning point k_{t2} is also represented by

$$\psi(k) = \langle g_{01}|k_0,k\rangle - i\langle g_{01}|k_0,k_{t2}\rangle\langle g_{02}|k_{t2},k\rangle. \tag{4-44}$$

Here, we used the symbolic notation

$$\langle g_{01}|k_0,k\rangle \equiv \exp[-i\int_{k_0}^{k} g_{01}(k)dk]. \tag{4-45}$$

Since the solutions (4-43) and (4-44) should be identical as mentioned before, we obtain the relation

$$\exp[i\int_{k_{t1}}^{k_{t2}}(g_{02}-g_{01})dk] = 1, \tag{4-46}$$

which gives

$$\int_{k_{t1}}^{k_{t2}}(g_{02}-g_{01})dk = 2(n+1)\pi. \tag{4-47}$$

Substitution of the expressions for g_0 and g_1 into (4-47) yields the quantization condition (4-40).

4-2-2 Asymptotic behavior near turning point

Although we can determine the structure of eikonal function g=g (k) by solving the relation (4-17), $H(k,g_0;\omega)=0$ for ω =fixed, we here consider an asymptotic behavior of waves in a case where one of the turning point locates at ($g_t,k_t=0$). We expand the Hamiltonian $H(k,g_0;\omega)=0$ around the turning point as

$$H(k,g_0;\omega) \cong \left(\frac{\partial H}{\partial g_0}\right)(g_0-g_t) + \frac{1}{2}\left(\frac{\partial^2 H}{\partial k^2}\right)k^2 + \cdots, \tag{4-48}$$

which yields

$$g_0 - g_t = -\frac{1}{2}\left(\frac{\partial^2 H}{\partial k^2}\right)\left(\frac{\partial H}{\partial g_0}\right)^{-1} k^2. \qquad (4\text{-}49)$$

Noting that the contribution from g_1 becomes negligibly small because $\partial H/\partial g_0 \to \infty$ near the turning point ($g_t, k_t = 0$), we have the asymptotic form of the solution near the turning point in the following form

$$\phi(x) \approx \int dk \exp[ik(x - g_t) + i\frac{1}{6}\left(\frac{\partial^2 H}{\partial k^2}\right)\left(\frac{\partial H}{\partial g_0}\right)^{-1} k^3]. \qquad (4\text{-}50)$$

Introducing a new variable $z = \left[\frac{1}{2}\left(\frac{\partial^2 H}{\partial k^2}\right)/\left(\frac{\partial H}{\partial g_0}\right)\right]^{1/3} k$, we carry out the integration in (4-50) and finally obtain the asymptotic solution

$$\phi(x) \cong 2\pi F \cdot A_i[F(x - g_t)], \qquad (4\text{-}51)$$

with abbreviation of

$$F^3 \equiv \left(\frac{2\partial H}{\partial g_0}\right)\left(\frac{\partial^2 H}{\partial k^2}\right)^{-1},$$

where $A_i[z]$ is the Airy function. The leading term of Airy function has been already mentioned in (3-32) and (3-33) as

$$A_i(z) \propto \frac{1}{2}\pi^{-1/2} z^{-1/4} \exp(-\frac{2}{3} z^{3/2}) \quad , \text{ for } z>0,$$

$$A_i(z) \propto \pi^{-1/2}(-z)^{-1/4} \cos[\frac{2}{3}(-z)^{3/2} - \frac{\pi}{4}] \quad , \text{ for } z<0.$$

The asymptotic behavior of waves near turning point is essentially the same as that in the configuration space, which is shown in Fig.1.

4-2-3 Stability analysis of electrostatic waves for weakly dissipative cases

The wavenumber k, the frequency ω, and the eikonal function, which appear in the Hamiltonian (4-17) and the quantization condition (4-40), are complex, in general. When dissipative effects are weak, however, the imaginary part of $H(k, g_0; \omega)$, namely, H_i, is small compared with the real part H_r, provided k_r, $g_0(k)$ and ω are all real. In this case, the imaginary

part of ω, also becomes small, and we can expand (4-17) as

$$0 \approx H_0(k, g_{0r}; \omega_r) + (iH_i(k, g_{0r}; \omega_r) + i\omega_i \frac{\partial H_0}{\partial \omega_r} + g_{0i} \frac{\partial H_0}{\partial g_{0r}}), \tag{4-52}$$

where $g_0 = g_{0r} + g_{0i}$ and $\omega = \omega_r + i\omega_i$. The functions g_{0r} and g_{0i} are determined from the zeroth- and the first-order parts of (4-52) as

$$H_0(k, g_{0r}; \omega_r) = 0, \tag{4-53}$$

$$g_{0i} = -i\left(\frac{\partial H_0}{\partial g_{0r}}\right)^{-1}\left(\omega_i \frac{\partial H_0}{\partial \omega_r} + H_i\right). \tag{4-54}$$

Equation (4-53) can be solved by **orbit integration** and we obtain

$$\frac{dk}{dt} = \left(\frac{\partial H_0}{\partial g_{0r}}\right) \Big/ \left(\frac{\partial H_0}{\partial \omega_r}\right), \quad \frac{dg_{0r}}{dt} = -\left(\frac{\partial H_0}{\partial k}\right) \Big/ \left(\frac{\partial H_0}{\partial \omega_r}\right), \tag{4-55}$$

provided that the initial values of k and g_{0r} satisfy the relation, $H_0(k(t=0), g_{0r}(t=0); \omega_r) = 0$. Then, the zeroth-order quantization condition reduces to

$$\oint g_{0r} \frac{dk}{dt} dt = 2(n + \frac{1}{2})\pi, \tag{4-56}$$

which determines the real frequency ω_r and the first-order quantization condition gives the following growth rate ω_i as

$$\omega_i = -\left(\oint H_i \Big/ \frac{\partial H_0}{\partial g_{0r}} dt\right)\left(\oint dt\right)^{-1}. \tag{4-57}$$

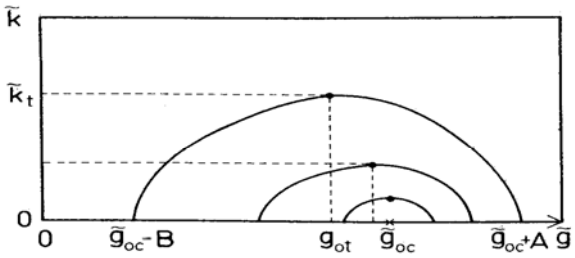

Fig. 12 Relation for g_0 vs. k for given values of frequency ω_r are shown. Several contour lines express the constant ω_r surfaces. The turning points in (g_0, k) plane is also illustrated and g_{0c} and k_t are the position of localization center and typical wavenumber, respectively.

Let us explain briefly the physical picture how to look at Fig.12. Corresponding mode is purely oscillatory between $-k_t$ and k_t, and must be exponentially increasing or decreasing as one moves away from a turning point. Therefore, the wave changes from one to the other when crossing turning points. The left hand side of (4-40) corresponds to the area covered by the contour for fixed frequency ω_r. We can determine the eigenfrequency from the quantization of the area covered by the contour. In practice, we first solve (4-55) numerically using Runge-Kutta method, and then determine the eigenfrequency and the growth rate from (4-56) and (4-57).

As an example, the present eigenmode analysis has been applied to the electrostatic drift waves. It has been pointed out in [2] that without the magnetic shear effect, drift waves may be localized in the following two cases:(1) drift frequency has a peak at a critical position of plasma density, (2) drift frequency does not have a peak for all positions, but the quasi-neutrality condition is not imposed. Therefore, whether drift waves are localized or not, depends sensitively on the density profile. We apply the numerical treatment of drift waves in the case of (1) by following the procedure mentioned in this chapter and we also can discuss analytical treatment of drift waves in case of (2) by expanding the Hamiltonian $H(k,g_0;\omega)$ around the localization center g_{0c} because the structure of $g_0(k)$ is symmetrical around the localization center and the structure becomes highly symmetrical as $k_\perp\rho$ is increased.[1,10]

4-2-4 Eikonal function in k-space and solution of integral equation (electromagnetic modes)

We here consider inhomogeneous plasma in the x-direction but is uniform in the y-z plane and expand the electric field vector in the following Fourier series,

$$\vec{E}(\vec{r},t)=\int_{-\infty}^{\infty}dk\vec{E}(k,k_\perp,k_{//};\omega)\exp[i(kx+k_\perp y+k_{//}z-\omega t)]. \qquad (4\text{-}58)$$

The integral equation for electromagnetic waves can be derived from the Vlasov-Maxwell equations, which is given in the following vectorial form (see, Eq.4-8, [34])

$$\int_{-\infty}^{\infty} \ddot{K}(k,k') \cdot \vec{E}(k') dk' = 0, \tag{4-59}$$

where the kernel $\ddot{K}(k,k')$ is a metric tensor and other arguments are suppressed for simplicity. It is convenient to introduce an eikonal function g (k) in the wavenumber space in the similar way as (4-12)

$$\vec{E}(k) = \vec{R}(k) \exp[-i \int g(k'') dk], \tag{4-60}$$

where $\vec{R}(k)$ is the polarization vector, which is assumed to vary slowly as a function of k. By expanding $\vec{R}(k)$ and $g(k'')$ in powers of $(k_0 L)^{-1}$, where $k \approx k_0$, k_0 is a typical wavenumber under consideration, we have

$$\vec{E}(k') = [\vec{R}(k) + (k-k') d\vec{R}/dk + \cdots] \exp\left\{-i \int^{k} g(k'') dk'' - i(k'-k) g(k) - 1/2 (k'-k)^2 g'(k) + \cdots\right\}$$

$$= \left\{\vec{R}(k) - \frac{i}{2}(k'-k)^2 g'(k) \vec{R}(k) + (k'-k) d\vec{R}/dk + O([kL]^{-2})\right\}$$

$$\times \exp\left\{-i(k'-k) g(k) - i \int^{k} g(k'') dk''\right\}, \tag{4-61}$$

where we used the following ordering, namely, $g/L \cong O(1)$, $(k'-k)^2 g'(k) \cong O([kL]^{-1})$. Substitution of (4-61) into (4-59) and neglecting the terms of order $(kL)^{-2}$ yield the equation determining the eikonal function g (k) as

$$0 = \ddot{H}(k,g) \cdot \vec{R}(k) + \frac{i}{2} \frac{\partial^2 \ddot{H}}{\partial g^2} \cdot \vec{R}(k) g'(k) + i \frac{\partial \ddot{H}}{\partial g} \frac{d\vec{R}(k)}{dk}, \tag{4-62}$$

where we used the notation

$$\ddot{H}(k,g) = \int_{-\infty}^{\infty} dk' \ddot{K}(k,k') \exp[-i(k'-k) g(k)]. \tag{4-63}$$

We note that physically, $\ddot{H}(k,g)$ corresponds to the local dispersion tensor in the WKB approximation and (4-63) determines the eikonal function g (k) correct up to the order $(kL)^{-1}$ for given eigenfrequency ω.

The boundary condition for the solution to be localized, is given as $\vec{E}(k) \to 0$ at $k \to \pm\infty$. For the case where there exist two turning points in

the k-space, the condition determining the eigenfrequency is written by the following the quantization condition

$$\oint_{\Gamma} g(k)dk = 2n\pi, \quad (\text{n=0, 1, 2}\cdots), \tag{4-64}$$

which is essentially same as (4-39) for the electrostatic modes. Let us next explain the actual method how to obtain g (k). Expanding $\vec{R}(k)$ and g (k) as

$$\vec{R}(k) = \vec{R}_0(k) + \vec{R}_1(k) + O([kL]^{-2}),\ g(k) = g_0(k) + g_1(k) + O([kL]^{-2}). \tag{4-65}$$

Substituting (4-65) into (4-62), we obtain from the order unity

$$\ddot{H}(k,g)\cdot\vec{R}_0(k) = 0, \tag{4-66}$$

and we also get from the order $(kL)^{-1}$

$$g_1(k)\frac{\partial\ddot{H}(k,g_0)}{\partial g_0}\cdot\vec{R}_0(k) + \ddot{H}(k,g_0)\vec{R}_1(k) + \frac{i}{2}\frac{\partial^2\ddot{H}(k,g_0)}{\partial {g_0}^2}\cdot\vec{R}_0(k)g_0'(k)$$

$$+\frac{\partial\ddot{H}(k,g_0)}{\partial g_0}\cdot\frac{d\vec{R}_0(k,g_0)}{dk} = 0. \tag{4-67}$$

The function $g_0(k)$ is determined from (4-66) as

$$0 = D(k,g_0) \equiv dey\{\ddot{H}(k,g_0)\}, \tag{4-68}$$

and $\vec{R}_0(k)$ is given as the right eigenvector of $\ddot{H}(k,g_0)$. We can also define the left eigenvector $L_0(k)$, which is given as

$$\vec{L}_0(k)\cdot\ddot{H}(k,g_0) = 0. \tag{4-68}$$

Taking scalar product of $\vec{L}_0{}^T(k)$ to (4-67) and using the relation (4-68), we get the equation for $g_1(k)$ as

$$g_1(k) = -i\frac{(1/2)\vec{L}_0{}^T\cdot(\partial^2\ddot{H}/\partial {g_0}^2)\cdot\vec{R}_0 g_0{}' + \vec{L}_0{}^T\cdot(\partial\ddot{H}/\partial g_0)\cdot(d\vec{R}_0/dk)}{\vec{L}_0{}^T\cdot(\partial\ddot{H}/\partial g_0)\cdot\vec{R}_0}. \tag{4-69}$$

We note that (4-29) can be derived from the compatibility condition where $\vec{R}_1(k)$ should be finite. Noting that $\ddot{H}(k,g_0)$ can be denoted by the 3×3 matrix as

$$\ddot{H} = \begin{pmatrix} a_{11} & a_{12} & a_{13} \\ a_{21} & a_{22} & a_{23} \\ a_{31} & a_{32} & a_{33} \end{pmatrix}, \tag{4-70}$$

we can write $\vec{L}_0{}^T(k)$ and $\vec{R}_0(k)$ from the cofactor forms of the matrix (4-70)

as

$$\vec{\vec{R}}_0 = \begin{pmatrix} A_{11} \\ A_{12} \\ A_{13} \end{pmatrix}, \quad \vec{L}_0{}^T = \begin{pmatrix} A_{11} & A_{21} & A_{31} \end{pmatrix}. \tag{4-71}$$

Noting the relation, $\sum_{i=1}^{3} a_{ij} A_{ji} = \delta_{ij} D(k,g)$, we get the relation for any set of k and g in the form

$$\vec{\vec{H}} \cdot \vec{\vec{R}}_0 = \begin{pmatrix} D \\ 0 \\ 0 \end{pmatrix}, \quad \vec{L}_0{}^T \cdot \vec{\vec{H}} = \begin{pmatrix} D & 0 & 0 \end{pmatrix}. \tag{4-72}$$

Differentiation of (4-72) with respect to g and taking the scalar product of these relations with $\vec{L}_0{}^T(k)$ yields the following relations

$$L_0{}^T \cdot \vec{\vec{H}}_g \cdot \vec{\vec{R}}_0 = A_{11} \frac{\partial D}{\partial g} - D \frac{\partial A_{11}}{\partial g}, \; L_0{}^T \cdot \vec{\vec{H}}_{gg} \cdot \vec{\vec{R}}_0 = -2 L_0{}^T \cdot \vec{\vec{H}}_g \cdot \vec{\vec{R}}_{0g} + A_{11} \frac{\partial^2 D}{\partial g^2} - D \frac{\partial^2 A_{11}}{\partial g^2}. \tag{4-73}$$

From (4-73) and the relation,

$$\frac{d\vec{\vec{R}}_0}{dk} = \frac{\partial \vec{\vec{R}}_0}{\partial k} + g_0{}' \frac{\partial \vec{\vec{R}}_0}{\partial g_0},$$

we can rewrite (4-69) in the following form

$$g_1 = -i \frac{\frac{1}{2} \frac{\partial^2 D}{\partial g_0{}^2} g_0{}' + L_0{}^T \cdot \vec{\vec{H}}_{0g} \cdot \frac{\partial \vec{\vec{R}}_0}{\partial k} A_{11}{}^{-1}}{\frac{\partial D}{\partial g_0}}. \tag{4-74}$$

We finally summarize briefly the procedure how to obtain the eigenfrequency:

(1) Given an integral kernel $\vec{\vec{K}}(k,k')$,

(2) Calculate the local dispersion relation from (4-63),

(3) Solve (4-68) for g_0 and calculate g_1 from (4-69) or (4-74) for given frequency ω,

(4) Substitution of these results into the quantization condition (4-64).

Numerical scheme to obtain the eigenfrequency has been discussed in detail in the reference [32].

4-3. Direct numerical integration method

We here discuss the numerical methods to solve the linear integral equation and/or integral-differential equations. An integral equation is a functional equation involving integral transforms of the unknown function $\phi(x)$. If the functional equation also involves a derivative of $\phi(x)$, the equation reduces to an integro-differential equation. A given integral equation is **homogeneous** if and only if every multiple $\alpha\phi(x)$ of any solution $\phi(x)$ is a solution. The linear integral equations are given in the following form

$$\beta(x)\phi(x) - \lambda\int_V K(x,\xi)\phi(\xi)d\xi = F(x), \qquad (4\text{-}3\text{-}1)$$

where $K(x,\xi)$, $\beta(x)$ and $F(x)$ are given functions, and the integration domain V may be given (Fredholm-type integral equations) or variable (e.g., Volterra-type integral equations). Three types of problems arise:

(1) **A linear integral equation of the first kind**, where $\beta(x)\equiv 0$, $\lambda = 1$, requires one to find an unknown function $\phi(x)$ with the given integral transform F (x). The corresponding operator equation $K\phi = F$ is analogous to a matrix equation.

(2) **A homogeneous linear integration of the second kind**, where $F(x)\equiv 0$, $\beta(x)\equiv 1$, λ is unknown, represents an *eigenvalue problem*. The corresponding operator equation $\lambda K\phi = \phi$ is analogous to a matrix equation.

(3) **A nonhomogeneous linear integration of the second kind,** where $\beta(x)\equiv 1$, λ is given, may be written as $\phi - \lambda K\phi = F$.

It should be noted that if $\beta(x)$ is a real positive function throughout V, one can reduce the general linear integral equation (4-3-1) to a linear integral equation of the second kind with the following transformation

$$\phi(x) = \frac{\bar{\phi}(x)}{\sqrt{\beta(x)}},\ F(x) = \bar{F}(x)\sqrt{\beta(x)},\ K(x,\xi) = \bar{K}(x,\xi)\sqrt{\beta(x)\beta(\xi)}. \qquad (4\text{-}3\text{-}2)$$

We note that these three types of problems are discussed in detail in the references [36,37]. Since the integral equation under consideration such as (4-3) and (4-59) is a linear homogeneous Fredholm type of equation, we hereafter restrict the present discussion to this case and briefly sketch the procedure how to solve the equation.

We here discuss the problem in the following two different approaches, namely, (1) method based on Gaussian quadrature [38], (2) method using orthogonal basis sets [11].

(1) Method based on Gaussian quadrature

We consider a simplified linear homogeneous Fredholm type of equation, which is given as

$$K\phi = \lambda\phi \ , \tag{4-3-3}$$

where K is an integral operator and λ is the eigenvalue. An approximate solution ϕ_N can be written as an expansion in terms of known functions [See, 38]

$$\phi_N = \sum_{j=1}^{N} a_j \chi_j \ , \tag{4-3-4}$$

where the χ_j may be Chebyshev polynomials, trigonometric functions, splines, etc. In practice, the choice of the χ_j is important in determining the numerical accuracy obtainable for a given value of N. [39] In order to calculate the a_j in (4-3-4), we employ the Raleigh-Ritz (or Galerkin) method and construct the quadratic form

$$I[\phi_N] = \frac{\sum_{i=1}^{N}\sum_{j=1}^{N} a_i a_j \int dkdk' \chi_i(k) K(k,k') \chi_j(k')}{\sum_{i=1}^{N}\sum_{j=1}^{N} a_i a_j \int dkdk' \chi_i(k) \chi_j(k')}. \tag{4-3-5}$$

The best choice for the a_j is obtained by making $I[\phi]$ extremal and results in the following system of linear algebraic equations:

$$(H_{ij} - \lambda M_{ij}) a_j = 0 \ \ (i,j = 1,.....N), \tag{4-3-6}$$

with abbreviations

$$H_{ij} = \int dkdk' \chi_i(k) K(k,k') \chi_j(k'), \tag{4-3-7}$$

$$M_{ij} = \int dkdk' \chi_i(k) \chi_j(k') \ . \tag{4-3-8}$$

In general, H_{ij} and M_{ij} are given, and λ and a_j have to be determined. In the case where H_{ij} is a function of ω(frequency of the mode), however, (4-3-6) can be rewritten as

$$A_{ij}a_j = 0,\ A_{ij} = H_{ij} - \lambda M_{ij}\ \ (i,j = 1,....N), \tag{4-3-9}$$

and then the frequency of the mode is now determined by the following condition

$$\det[A_{ij}] = 0. \tag{4-3-10}$$

If A_{ij} is large matrix, it might be convenient to solve the following equation instead of (4-3-10)

$$\det[A_{ij} - \mu(\omega)\delta_{ij}] = 0, \tag{4-3-11}$$

and we determine the values of ω to realize the relation $\mu(\omega) = 0.$

(2) **Method based on representation in an orthogonal basis set**

It should be noted that the method under consideration differs from the approach based on Gaussian quadrature discussed before. We decompose the radial eigenfunction into its representation in an orthogonal basis set, chosen according to satisfying two conditions: (a) the basis functions exhibit the same asymptotic behavior as the radial eigenfunction, and (b) the choice allows the k-space integration analytically. We choose the associated Laguerre functions

$$\tilde{L}_p{}^{\mu}(x) = [p!/(p+\mu)!]^{1/2} x^{\mu/2} e^{-x/2} L_p{}^{\mu}(x), \tag{4-3-12}$$

where $L_p{}^{\mu}$ is the usual Laguerre polynomial and the normalization has been chosen such that

$$\int_0^{\infty} dx \tilde{L}_n{}^{\mu}(x)\tilde{L}_m{}^{\mu}(x) = \delta_{n,m}. \tag{4-3-13}$$

Substituting the following function

$$\psi_m(k) = \sum_{p=0}^{\infty} W_p \tilde{L}_p{}^{|m|}(k^2R^2), \tag{4-3-14}$$

into (4-5)(see, page 21) and operating on the both sides with $\int_0^{\infty} dkk\tilde{L}_q{}^{|m|}(k^2R^2)$, gives the following matrix equation

$$\vec{M}\cdot\vec{W} = 0, \tag{4-3-15}$$

where

$$\bar{M}_{pq} = (k_{//}{}^2 R^2 + 2p + |m| + 1)\delta_{p,q} - \sqrt{(p+1)(p+|m|+1)}\,\delta_{p,q-1}$$
$$-\sqrt{p(p+\mu)}\,\delta_{p.q+1} + \sum_j \frac{k_{Dj}{}^2 R^2}{2} \sum_l B_{jl} D_{pq}{}^l(\varepsilon_j), \qquad (4\text{-}3\text{-}16)$$

with

$$D_{pq}{}^l(\varepsilon) = \int_0^\infty dx \int_0^\infty dx' \tilde{L}_p{}^{|m|}(x) \tilde{L}_q{}^{|m|}(x') I_l(\varepsilon\sqrt{xx'}) I_{l+m}[(1-\varepsilon)\sqrt{xx'}] e^{-(x+x')/2}. \quad (4\text{-}3\text{-}17)$$

It should be noted that $D_{pq}{}^l$ is independent of ω, so that it need only be calculated once foe a given azumuthal quantum number m. This matrix equation is truncated and solved for the eigenvalues $\omega_{m,n}$ and the eigenfunctions $W_{m,n}$ in (4-3-15) which determines the solutions of the integral equation. The eigenfunctions in k-space are reconstructed using (4-3-14). Once we obtain the eigenfunction in k-space, the real space eigenfunctions are recovered from the relation

$$\int_0^\infty dx \tilde{L}_n{}^m(x) J_m(\sqrt{xy}) = 2(-1)^n \tilde{L}_n{}^m(y), \qquad (4\text{-}3\text{-}18)$$

and then we finally have the solution

$$\phi_m(r) = \frac{im}{R^2} \sum_p (-1)^p W_p \tilde{L}_p{}^{|m|}\left(\frac{r^2}{R^2}\right). \qquad (4\text{-}3\text{-}19)$$

Varying the size of the truncated matrix and noting the sensitivity of the eigenfrequencies and eigenfunctions to this change may test the numerical convergence of this method.

4-4 Extension of ray tracing theory for inhomogeneous plasmas based on eikonal function formula

Traditional approach to study the wave propagation in inhomogeneous plasmas is based on the so-called geometrical optic approximation. However, it is well known that this approach based on the ray tracing equation and the wave energy conservation equation is not always convenient for numerical computation because the conservation equation is the partial differential equation. Since the present approach is based on the integral

equation in the k-space, the formula may include a couple of kinetic effects such as the finite Larmor radius effect, cyclotron and Landau damping effects etc.

Following the discussions in Chapter4.2, we explain briefly an extended ray tracing formula [40]. We here consider the following case

$$\phi(\vec{x}) = \int d^3k e^{i\vec{k}\cdot\vec{x}}\phi(\vec{k}), \qquad (4\text{-}4\text{-}1)$$

$$\vec{k}^2\phi(\vec{k}) = \int d^3k K(\vec{k},\vec{k}')\phi(\vec{k}') \ , \qquad (4\text{-}4\text{-}2)$$

which corresponds to the case of $F(k) = k^2$ in ((4-3)[see, Chapter4.1]. Introducing the eikonal function

$$\phi(k) = \exp[-iS(\vec{k})], \qquad (4\text{-}4\text{-}3)$$

where the eikonal function $S(k)$ is determined by the following equations

$$H(\vec{k},\vec{G}) = 0, \qquad (4\text{-}4\text{-}4)$$

$$\nabla_k S_1 \cdot \frac{\partial H(\vec{k},\vec{G})}{\partial G} + \frac{1}{2}\sum_{j,l=1}^{3}\frac{\partial^2 H}{\partial G_j \partial G_l}\frac{\partial^2 S_0}{\partial k_l \partial k_j} = 0, \qquad (4\text{-}4\text{-}5)$$

with the abbreviations of

$$H(\vec{k},\vec{G}) = \int K(\vec{k},\vec{k}')e^{-i(\vec{k}-\vec{k}')\cdot\vec{G}}d^3\vec{k}' - \vec{k}^2, \qquad (4\text{-}4\text{-}6)$$

$$S(k) = S_0(k) + S_1(k) + O[(kL)^{-2}], \qquad (4\text{-}4\text{-}7)$$

$$\vec{G} \equiv \vec{\nabla}_{\vec{k}} S_0(\vec{k}). \qquad (4\text{-}4\text{-}8)$$

Substitution of (4-4-3) into (4-4-1) and carrying out the integral by the steepest descent method, which have been discussed in Chapter4.3 of "Sokendai Lecture Note-I", gives the following wave propagation formula

$$\phi(\vec{x}) = A(\vec{x})e^{i\varphi(\vec{x})}, \ A(\vec{x}) = (-i2\pi)^{1/2}[\det(P_{jl})]^{-1/2}e^{-iS_1(\vec{k})} \ , \qquad (4\text{-}4\text{-}9)$$

$$\varphi(\vec{x}) = \vec{k}\cdot\vec{x} - S_0(\vec{k}), \ \vec{x} = \vec{G}, \ P_{jl} \equiv \frac{\partial^2 S_0}{\partial k_j \partial k_l} \ (j,l = 1,2,3). \qquad (4\text{-}4\text{-}10)$$

As mentioned before, (4-4-6) can be regarded as the Hamiltonian-Jacobi equation of the classical dynamics. Therefore, the quantities $\vec{k}$ and $\vec{G}$ are determined by a numerical integration of the "Hamiltonian system"

$$\frac{d\vec{k}}{d\tau} = -\frac{\partial H}{\partial \vec{G}}, \ \frac{d\vec{G}}{d\tau} = \frac{\partial H}{\partial \vec{k}}, \qquad (4\text{-}4\text{-}11)$$

which is essentially the same as (4-55). The other amplitude and phase factors φ, S_1 and P_{jl} are obtained by the numerical integration of the following ordinary differential equations

$$\frac{d\varphi}{d\tau} = \vec{k} \cdot \frac{\partial H}{\partial \vec{k}}, \tag{4-4-12}$$

$$\frac{d\vec{S}_1}{d\tau} = \frac{i}{2} \sum_{j,l=1}^{3} \frac{\partial^2 H}{\partial G_j \partial G_l} P_{jl}, \tag{4-4-13}$$

$$\frac{dP_{jl}}{d\tau} = \frac{\partial^2 H}{\partial k_j \partial k_l} + \sum_{m=1}^{3} \left[\frac{\partial^2 H}{\partial k_j \partial G_m} P_{ml} + \frac{\partial^2 H}{\partial k_l \partial G_m} P_{mj} \right] + \sum_{m.n=1}^{3} \frac{\partial^2 H}{\partial G_m \partial G_n} P_{nl} P_{mj}. \tag{4-4-14}$$

It should be noted that the profiles of amplitude and phase of the wave could be determined by the local dispersion relation $H(\vec{k},\vec{G}) = 0$. As an example, the wave fronts and ray trajectories of electromagnetic modes radiated from a local source in an inhomogeneous magnetoplasma waveguide are studied numerically using the extended ray tracing theory just discussed in this chapter. Typical ray trajectories (solid lines) and wave fronts (dotted lines) of an electromagnetic mode radiated from a local source below the electron cyclotron frequency in an inhomogeneous magnetoplasma are shown in Fig.13.

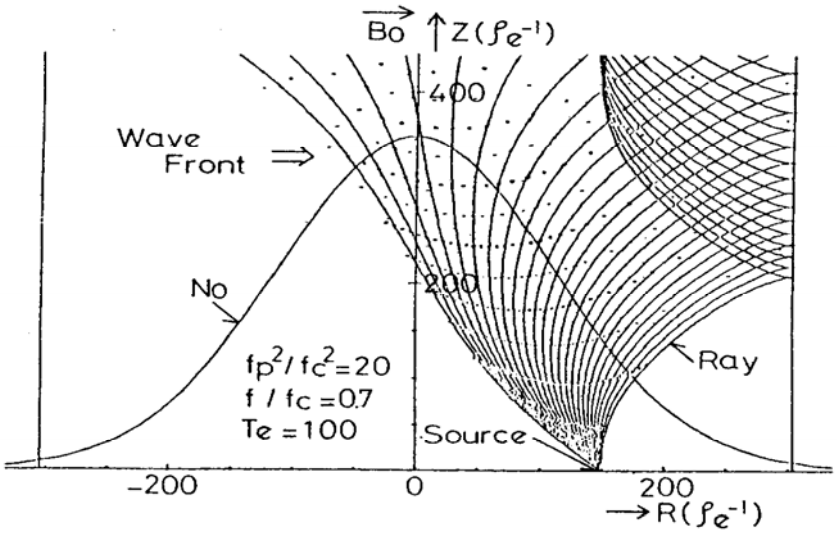

Fig.13 Wave fronts and ray trajectories of an electromagnetic mode. Radiating source location is not at the plasma center. [Ref.41]

Reflection and refraction of the radio-frequency field are clearly shown in this figure. The reflection may occur at the electron plasma frequency

layer, which is the same as that of he resonance cone fields observed experimentally [42]. As was shown in Fig.13, the reflections of the electromagnetic waves lead the trapping of the modes in the inhomogeneous magnetoplasma and the repetition of those reflections results in a plasma waveguide.

5. Examples of Nonlocal Stability Analysis based on Integral Equation in K-space

5-1. Example of WKB -type eigenmode analysis

We first discuss the WKB-type of eigenmode analysis for collisionless drift waves using the formula discussed in Sec.4-2-3. Typical results for $\tilde{g}_0(k)$ for values of ω_r/ω_{*i}, where ω_{*i} is the ion diamagnetic drift Frequency, corresponding to given radial mode number are presented in Fig.14.

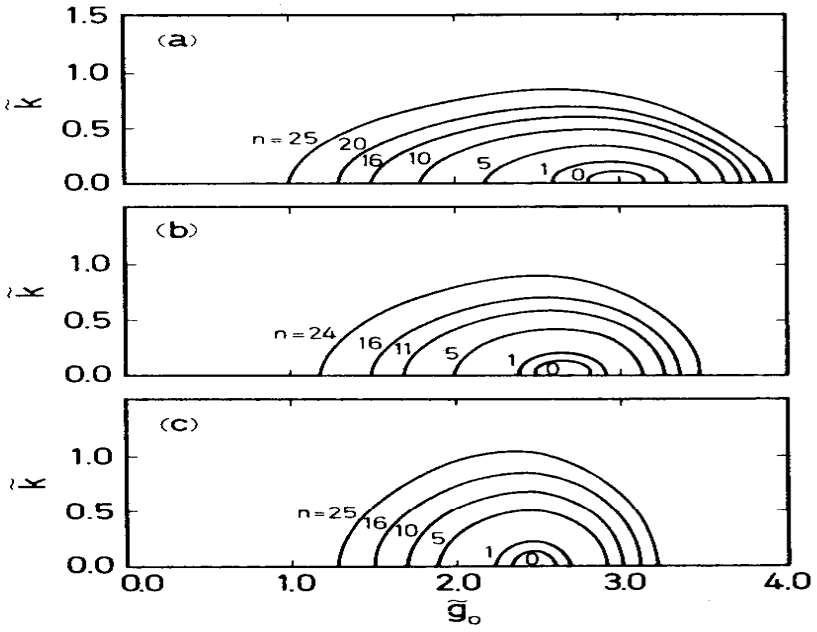

Fig.14 Results for $\tilde{g}_0(k)$ for given values of ω_r/ω_{*i} are shown for three cases, (a) $\rho_i k_\perp = 0.4$, (b) 0.8, and (c) 1.2, respectively. The parameters used are $\omega^2_{pi}/\omega^2_{ci} = 100$, $T_i/T_e = 1.0$, $\lambda/\rho_i = 100$, $k_{//}\rho_i = 10^{-3}$ (from [2]).

From this figure (Fig.14), we can determine the mode localization center, the localized region, and corresponding wavenumber, $\tilde{k} \equiv k\rho_i$. As shown there, the localization center shifts toward the high density side and the localized region becomes narrower as $\rho_i k_\perp$ increases. Also, it turns out that the wave structure becomes more symmetric around the localization center and the corresponding wavelength increases as $\rho_i k_\perp$ becomes large.

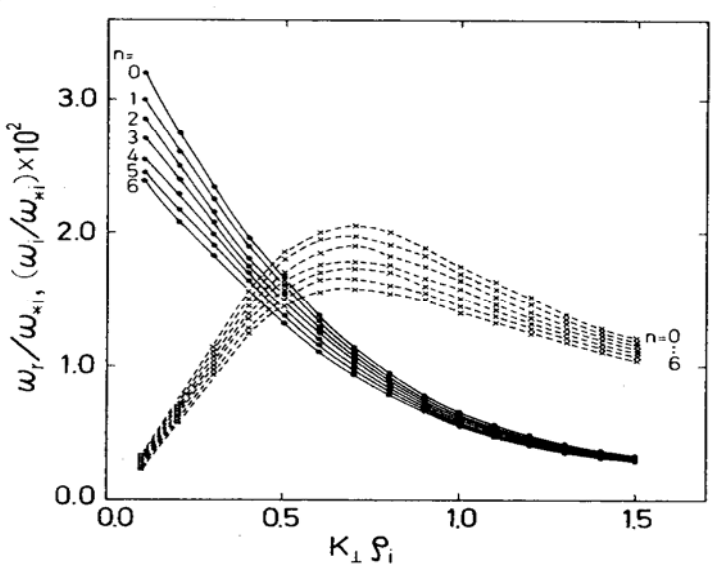

Fig.15 Results of ω_r/ω_{*i} (solid lines) and ω_i/ω_{*i} (dashed lines) vs. $\rho_i k_\perp$ for the mode numbers n=0-6 are illustrated. The parameters used here are the same ones in Fig.14(from [2]).

It turns out from the results in Fig.15 that the growth rate of the fundamental mode (n=0) is the largest one for these parameters.

5-2. Examples of eigenmode analysis based on representation in an orthogonal basis sets

Next, we introduce an example of the eigenmode analysis using the method based on the representation in an orthogonal basis set, which has been discussed in Sec.3-4-(2). To demonstrate this problem, we here consider a nonlocal analysis of drift and drift-cyclotron waves in cylindrical

geometry (see, Ref.11). The instability associated with the drift cyclotron wave arises from the coupling of an ion cyclotron (ion Bernstein) wave with an ion diamagnetic drift wave. The central cell region of mirror devices such as TMX was often predicted to be unstable to such drift cyclotron waves. We consider the following two cases, namely, drift cyclotron modes near threshold (Fig.16) and also far from threshold (Fig.17). In Fig.16 (a), the density scale length has been sufficiently shorted to cross the stability boundary and it allows coupling between the first three radial eigenmodes of the ion cyclotron branch and the drift wave branch.

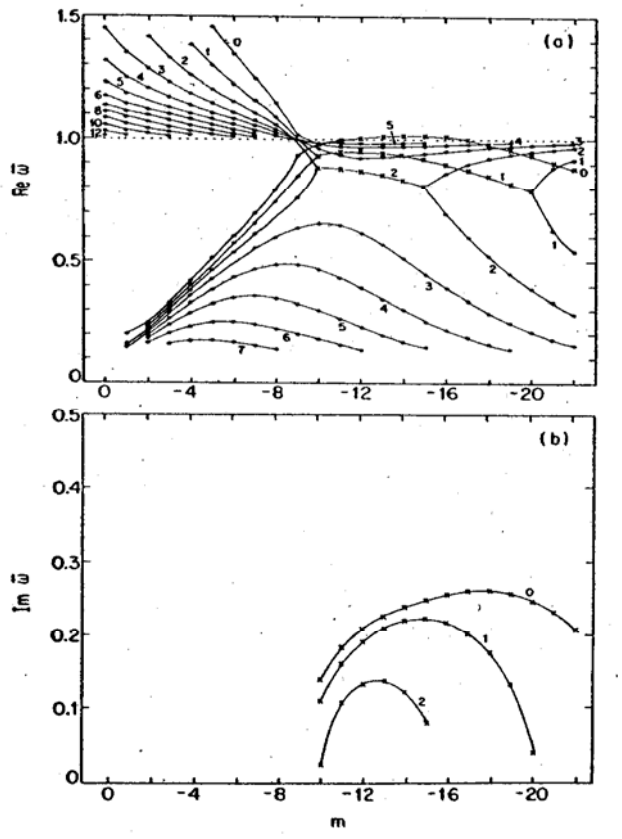

Fig.16 Dispersion relation for drift cyclotron modes near threshold for modes propagating in the ion diamagnetic direction (m<0). Crosses indicate the growing modes. $R/\rho_i = 3$ (R is the density scale length) and $\omega_{pi}^2/\Omega_i^2 = 50.$ (a)Real frequency versus m, (b) growth rate (imaginary frequency) versus m(from [11]).

As m increases, the fundamental mode (n=0) becomes unstable first, followed by n=1 and n=2. The corresponding growth rates for the unstable modes are plotted in Fig. 16 (b). In this case close to threshold, the fundamental mode is the most unstable and persistent mode. It should be noted from Fig. 16 that the lowest azimuthal mode number to support unstable modes is well approximated by

$$\frac{m\rho_i^2}{R^2} \cong 1 \ , \qquad (5\text{-}1)$$

which corresponds to the relation $\Omega_i \cong \omega_{*i}$ in local theories. The lowest stable radial eigenmode family is n=3 in the case of Fig. 16 (a), bounding the higher families below the ion cyclotron harmonic. Also, the eigenfrequencies of the higher radial eigenmode families always asymptote to the ion cyclotron harmonic. Since the term $(\omega - \omega_{*i})/(\omega + n\Omega_i)$ is involved in the local dispersion relation for the drift cyclotron wave [see the text book by K. Miyamoto, Ref. 43], the relation $\omega_{*i} \cong \Omega_i$ should be satisfied on $\omega \cong \Omega_i$ to avoid the divergence. From (5-1), we easily obtain m=9 for $R/\rho_i = 3$, which is shown in Fig. 16 (a).

Far above threshold (see. Fig. 17), many families of radial eigenmodes become unstable, with frequencies both above and below the ion-cyclotron frequency. The growth rates of the unstable modes are all of the same order, and can be as large as one-third of the real frequency. The most unstable mode is not the fundamental branch, nor is it the most persistent. The present results close to instability threshold (Fig. 16) indicate that what one would observe is a very narrow frequency, comprised of a number of fundamental radial eigenmodes with different azimuthal mode numbers. Away from threshold (Fig. 17), lots of unstable modes exist with growth rates all of the same order of magnitude. Assuming that these modes all saturate at approximately the same amplitude, the frequency spectrum would appear turbulent with a broad peak around the ion-cyclotron frequency. The eigenfunction calculations indicate a spatial structure characteristic of global modes, and are probably sensitive to the exact plasma profile. It should be pointed out that variation of the plasma density and magnetic

field along the plasma column introduces boundary conditions on $k_{//}$ that are not involved here.

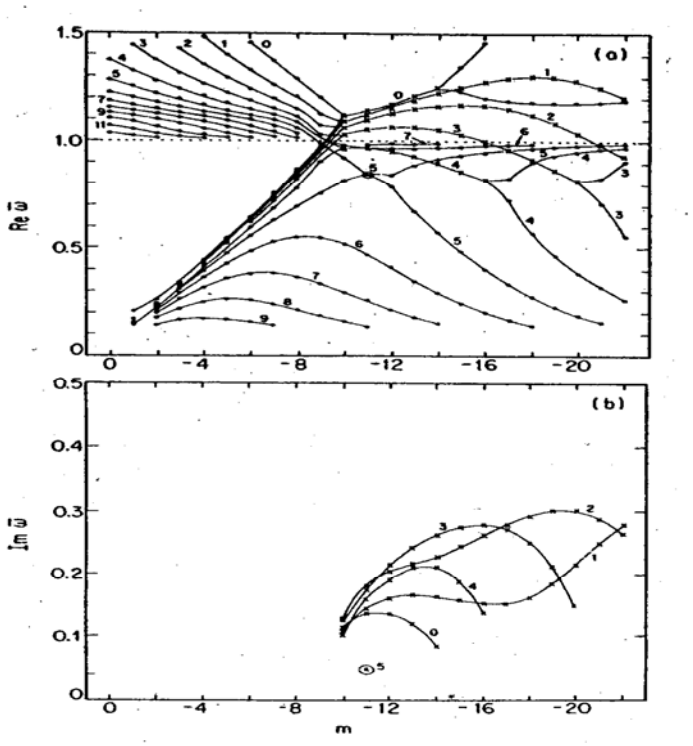

Fig. 17 Dispersion relation for drift-cyclotron waves far from threshold. Crosses indicate growing modes. $R/\rho_i = 3$ and $\omega_{pi}^2/\Omega_i^2 = 200.$
(a) Real frequency versus m. (b) Growth rate (imaginary frequency) versus m.

5-3. Comparison between experimental observation and theoretical results(Bumpy torus and mirror devices)

The cross field particle, momentum, and energy transport in magnetically confined toroidal plasmas generally exceeds neoclassical transport by more than one order of magnitude. Understanding and controlling such anomalous transport is one of the most important topics. There is strong experimental evidence that this anomaly can be attributed

to a small scale turbulent driven by gradients of plasma parameters such as density, temperature, velocity and so on. As was mentioned in the introduction, in the 1970's, electrons were found to be the main channel for energy loss. Therefore, the electron temperature gradient (ETG) driven instability was the plausible candidate for the anomalous transport. Later, in the early 1990's, it was found that ions became the energy loss channel in neutral beam injection (NBI) heating tokamak plasmas. Associated with these observations, the ion temperature gradient (ITG) driven instability has been studied intensively. Currently, it is widely accepted that linear and nonlinear theories and simulations for ITG instability are enough to explain the ion anomalous transport qualitatively and the ion thermal diffusivity reduces to the neoclassical level in advanced tokamak plasmas with internal transport barrier (ITB's). Recent experimental observations seem to indicate, however, that the electron thermal diffusivity is often still anomalous even in discharges with ITB.

Improvement of both theories and diagnostics with high spatial and temporal resolution really encourage definite comparison between theoretical predictions and experimental observations. We here show an example for comparison between theoretical prediction based on the nonlocal WKB analysis and experimental observation. The stability aspects associated with low frequency fluctuations have been investigated in ELMO Bumpy Torus (EBT) and Nagoya Bumpy Torus (NBT) experiments. The Heavy Ion Beam Probing (HIBP) has also measured potential profile in detail. In EBT and NBT, there are three typical operations, namely so-called quiescent mode (C-mode) operation, Torus mode (T-mode) operation and Mirror mode (M-mode) operation as the background pressure is decreased.
Also, the hot electron component is created by ECH second resonance heating, in other word, the radiation increases and the deep potential well is formed in the T-mode operation.

A typical example for these operations is shown in Fig.18. Low frequency fluctuation of density with 100 kHz, potential variation, and hot electron production (radiation power) are shown in Fig.18

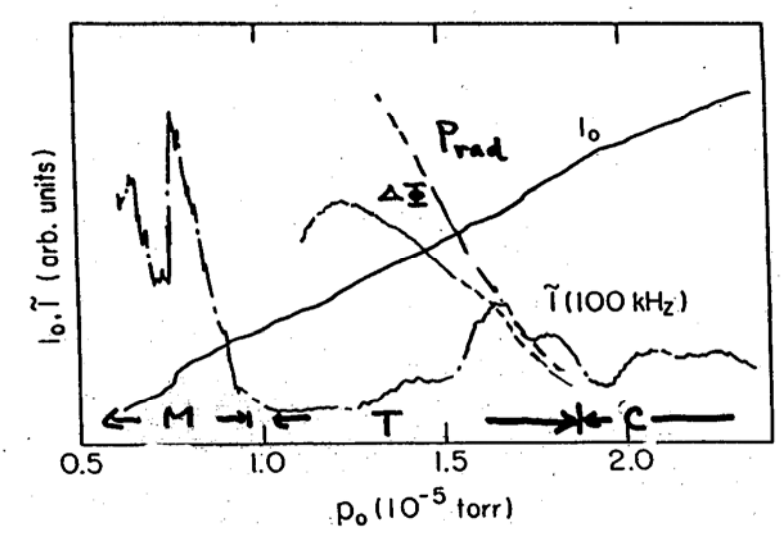

Fig.18 Density fluctuation (100 kHz), plasma potential, radiation power versus background pressure (C-, T- and M- modes) operations in NBT experiments.

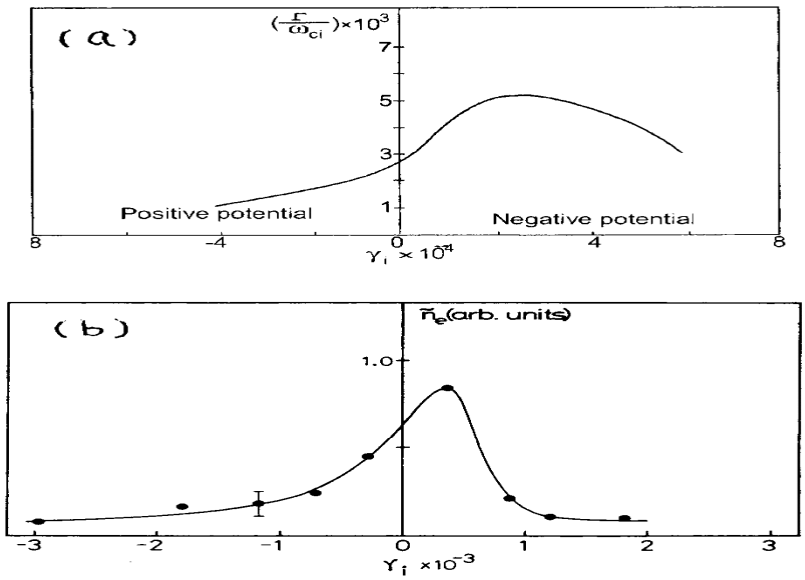

Fig.19 Normalized maximum growth rate of electrostatic drift mode versus $E \times B$ shear parameter $\gamma_i (= \omega_{Ei}^2 / \omega_{ci}^2)$. The result from WKB type solution based on integral eigenvalue equation (a)[Ref.10] and fluctuation level as a function of $\gamma_i (= \omega_{Ei}^2 / \omega_{ci}^2)$ observed in Gamma-10 mirror (b)[Ref.44].

Since the fluctuations with less than 100kHz as shown in Fig. 18 are strongly localized at the position of the steepest density gradient with $k_r\rho_i \leq 1$, we carried out the nonlocal stability analysis to study these fluctuation events and compared the theoretical results with experimental observations.

Since the low frequency fluctuations (electrostatic drift waves) are enhanced and then decrease at the T-mode operation and this enhanced fluctuations are correlated with deep potential wells as shown in Fig. 18, we consider the effect of ambipolar field on the electrostatic drift waves to explain these low frequency fluctuation phenomena as was seen in EBT and NBT experiments (see, Fig. 18).

The result of WKB type solution based on integral eigenvalue equation and fluctuation level observed in Gamma-10 mirror device are plotted as a function of $\gamma_i(=\omega_{Ei}^2/\omega_{ci}^2)$ in Fig. 19 (a) and Fig. 19 (b), respectively. As shown in Fig. 19, the most unstable situation is shifted toward somehow negative electric field side, where $E\times B$ drift cancels the electron diamagnetic drift. But the sheared flow, which is large enough compared to the diamagnetic drift, may enhance the perpendicular Landau damping (see, Ref. 5), and it may suppress the drift wave instability, regardless of its polarity of electric field. As shown in Fig. 19 (b), this theoretical prediction was confirmed by experimental observations in the Gamma-10 mirror experiment and also by the biasing experiment of Tokamak de Varennes. [Ref. 45]

5-4. Nonlocal ITG and ETG modes based on electrostatic, low β and full β models

There are remarkable improvements on methods how to solve the integral eigenmode equation. We discussed the effects of finite beta, magnetic shear, and perpendicular velocity shear on a couple of modes such as local slab short wavelength ion temperature gradient (SWITG) modes, nonlocal slab SWITG modes, electron temperature gradient (ETG) modes, nonlocal toroidal SWITG modes and so on. We here introduce some typical results, which are

obtained by the direct numerical integration method discussed in Sec. 4. We first explain briefly about SWITG modes. This mode is characterized by $\omega_r < 0$ and $|k_y \rho_i| > 1$. Normalized frequency and growth rate for the conventional ion temperature gradient (ITG) mode, SWITG mode, conventional electron temperature gradient (ETG) mode and SWETG mode are plotted in Fig. 20.

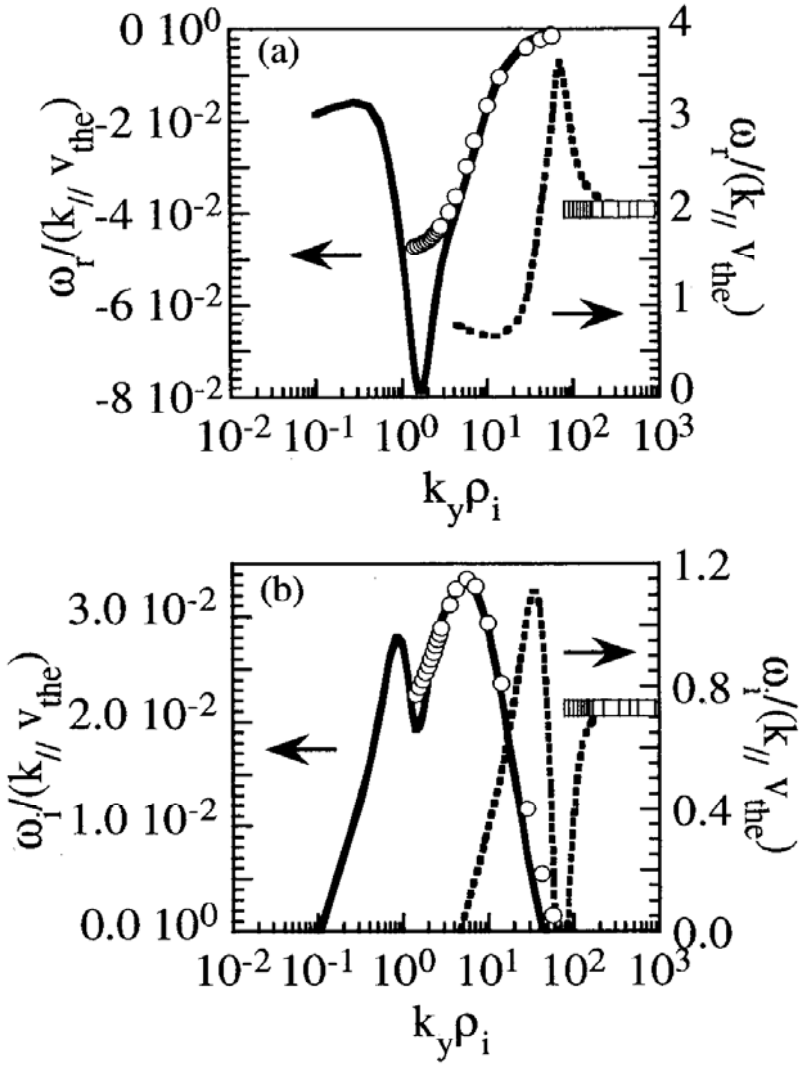

Fig. 20 Normalized frequency (a) and growth rate (b) for ITG (left panel) and ETG (right panel) modes. Solid line shows conventional ITG and SWITG modes and dotted line indicates conventional ETG and SWETG modes (from Ref. [46]).

It turns out from Fig. 20 that two new unstable branches exist in the regions $k_y\rho_i \geq 1$ and $k_y\rho_e \geq 1$. Since the wavelength of the SWITG mode is shorter than that of the conventional ITG mode, namely, $k_y\rho_i \geq 1$, we have to solve the eigenvalue problem based on integral equation instead of differential equation. The ITG mode may produce a significant level of anomalous transport, which is evaluated based on the so-called **mixing length theory**. Recently, it has been emphasized that the SWETG mode can be significantly modified by the Debye shielding effect and is strongly stabilized in high temperature plasma for $\lambda_D/\rho_e > 1$[12].

We next explain briefly the **Gyro-kinetic Integration Model**, which is composed of the gyro-kinetic equation together with the basic equations, namely Poisson's equation and the Ampere's law. The gyro-kinetic integration model is solved for following two configurations, namely for the sheared slab configuration (with magnetic gradient) and also for the toroidal configuration, where the ballooning representation for an axisymmetric toroidal geometry in $s-\alpha$ equilibrium is employed. Since both ions and electrons are assumed to be **nonadiabatic** in this model, the transit effect, finite Larmor radius effect, and curvature and magnetic gradient drifts are automatically included. The integral equation for the study of ITG modes in arbitrary beta plasmas is upgraded and employed for nonlocal study of short wavelength modes in a sheared slab model. In the nonlocal model, the parallel wave number, $k_{//} = (x/L_s)k_y$, where L_s is the magnetic shear length, is related to the mode structure and the cross-field wave number, $k_\perp = \sqrt{k_y^2 + k^2}$ includes poloidal and radial components. So, there are several distinctive modes with different spatial structure in different frequency regions. In the long wavelength regime $k_y\rho_i \leq 1$, the conventional ITG modes have been identified. A new series of short wavelength modes are also identified. For the nonlocal modes, we only set the k_y, whereas the k_x spectrum is determined by the solutions to the eigenmode equation.

Shown in Fig. 3 (a) are the eigenvalues of the dispersion equations for

$k_y\rho_e = 0.1$, i.e., S0, S1, C0, C1, and so on, in the complex plane of the frequency normalized to the electron diamagnetic drift frequency ω_{*e}. Also, the normalized growth rate of the nonlocal modes as function of $k_y\rho_e$.

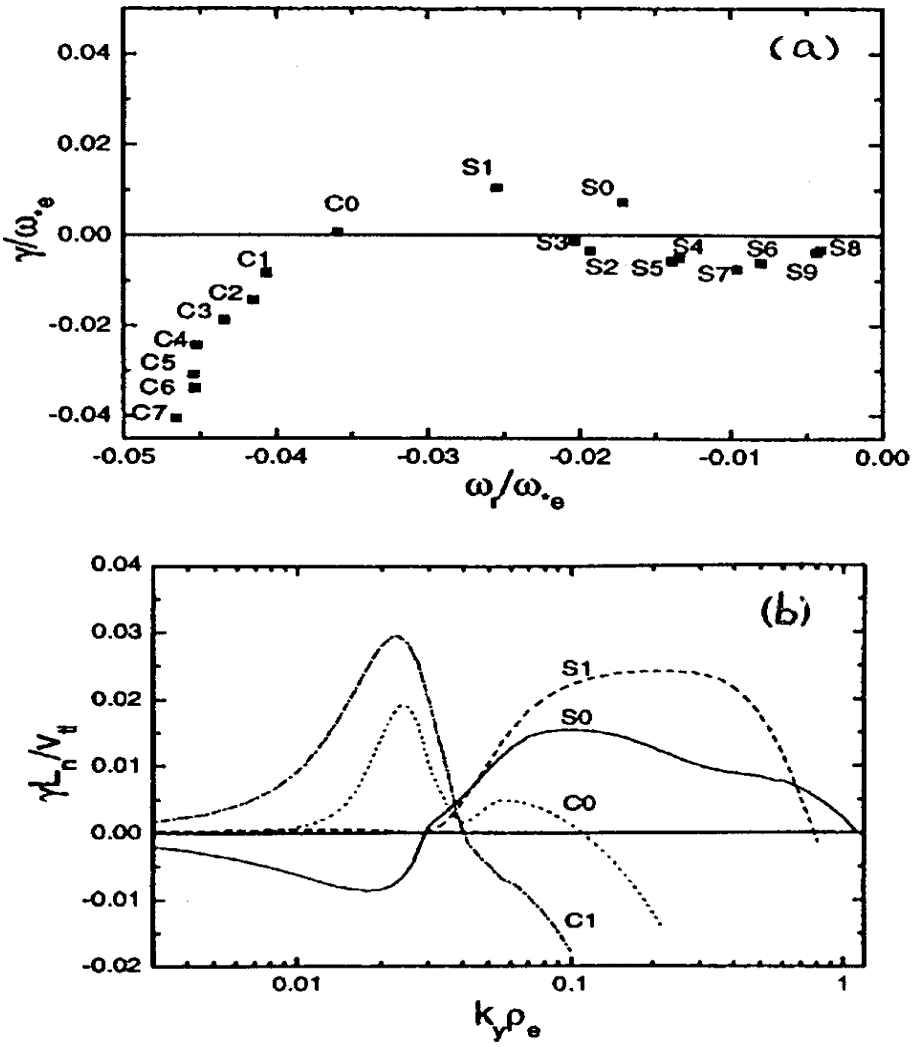

Fig. 21 Eigenvalues of the nonlocal modes (a). The letter C, and S denote different series and the numbers denote different harmonic order. Normalized growth rate of the nonlocal modes as functions of $k_y\rho_e$ (b) in case of $\beta = 0$. The solid, dashed, dotted, and dashed-dotted lines denote the S0, S1, C0, and C1 modes, respectively (from Ref. [13]).

In Fig. 21, we choose the parameters: $\eta_e = 2$, $\eta_i = 2$, $T_e/T_i = 1$, $m_i/m_e = 1836$, $L_n/L_s = 0.025$ and $k_y\rho_e = 0.1$. The even and odd numbers denote the even and odd modes, respectively. The mode structure becomes more complicated as the mode number increases. The solutions with higher frequencies, the C series as shown in Fig. 21 (a), seem to be on the short wavelength tai of the conventional ITG modes, e.g., the C0, C1, and C2 are verified to be the conventional ITG modes at $k_y\rho_e = 0.1$ with harmonic order number $l = 0, l = 1$, and $l = 2$, respectively. It should be noted that only the fundamental mode is unstable in the short wavelength regime for these parameters and higher order modes are rather stable. The low frequency modes, the S series, are the short wavelength modes. The k_y spectra of the lowest even and odd short wavelength modes are shown in Fig. 21 (b), together with those for the lowest even and odd conventional ITG modes.

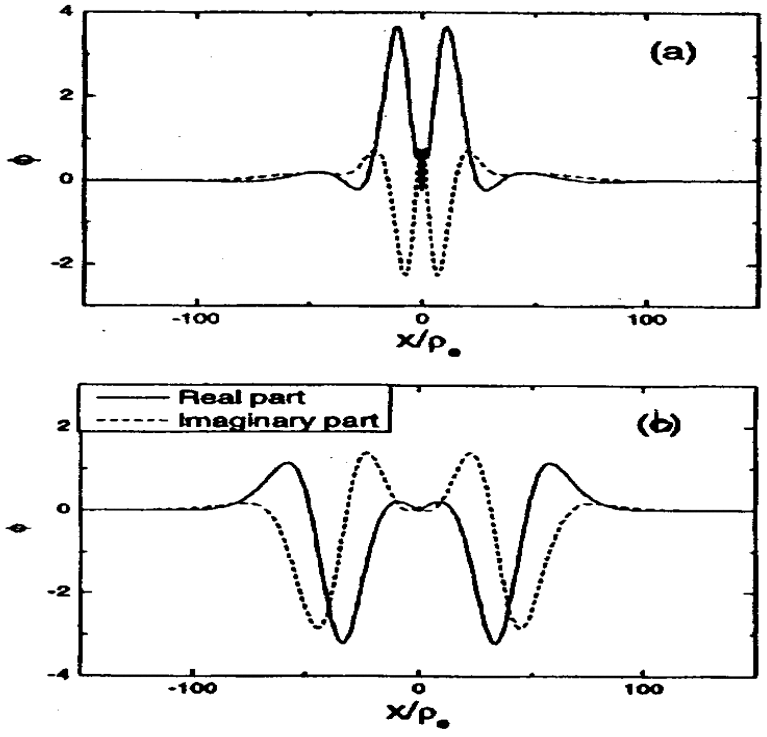

Fig. 22 Mode structures of the S0 and C0 in Fig. 22 (a) and Fig. 22 (b), respectively. The parameters used in Fig. 22 are same as Fig. 21. (from Ref. [13]).

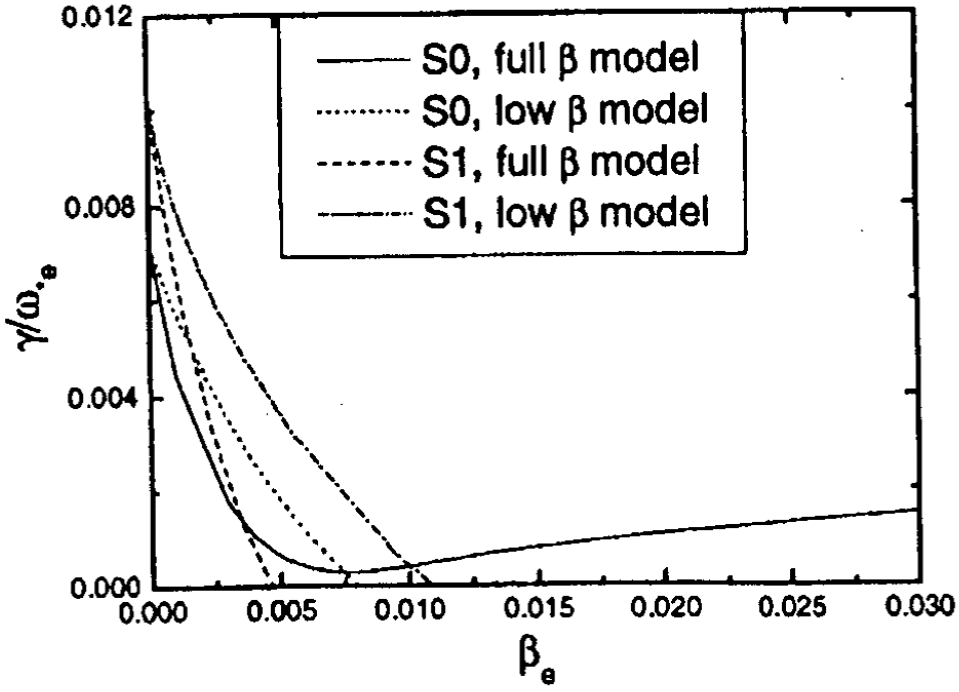

Fig. 23 Normalized growth rate as functions of β_e. Solid lines: the S0 mode from the full β model; dashed lines: the S1 mode from the full β model; dotted lines: the S0 mode from the low β model; dashed-dotted lines: the S1 mode from the low β model. The other parameters are the same as in Fig. 21(from [13]).

Shown in Fig. 23 are the growth rates of S0 and S1 modes as function of β_e, obtained from low β and full β models. It should be noted that only ϕ and $A_{//}$ components are involved in the low β model and the $A_{\perp}$ component in addition to ϕ and $A_{//}$ is also involved in the full β model. It turns out from Fig. 23 that the S1 mode may be stabilized by a finite β effect in both of the models. However, the fundamental mode cannot be stabilized by the β effect when the magnetic gradient effect is considered in the full β model. Therefore, the S1 mode is more unstable at the low β and weak magnetic shear regions than the fundamental. There is an obvious difference between the local and nonlocal results. The frequency of the local mode

is continuous as $b_i = (k_y\rho_i)^2/2$, while the conventional mode and the short wavelength mode are separated as shown in Fig.21 (b). However, the conventional and short wavelength modes couple to each other when η_e increases. Consequently, this coupling results in a continuous k_y spectrum with two humps in both short wavelength and long wavelength regimes. Local dispersion relation and simple eigenvalue analyses based on differential equations cannot discuss these nonlocal features of highly localized modes.

Although we discussed the $E \times B$ sheared flow effect on electrostatic drift wave, as was shown in Fig.19, we here discuss the effect of the effects of $E \times B$ sheared flow and β on the SWITG mode. A typical result is shown in Fig.24.

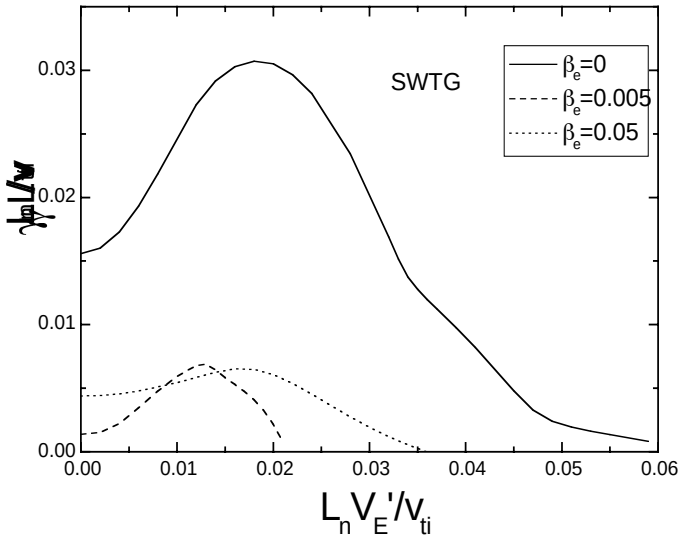

Fig.24 Normalized growth rate ($\gamma L_n/v_{ti}$) as functions of normalized shear flow velocity ($L_n V_E'/v_{ti}$) for $k_y\rho_i = 0.1$. The solid, dashed, and dotted lines denote the results for $\beta_e = 0, 0.005$ and 0.05, respectively. The parameters, $\eta_e = 2$, $\eta_i = 2$, $T_e/T_i = 1$, $m_i/m_e = 1836$, $L_n/L_s = 0.025$ and $\Omega_e^2/\omega_{pe}^2 = 1$ are employed(from [66]).

As was shown in Fig.24, the initial rise in V_E' causes an increase in the growth and a decrease in the frequency. The growth rate reaches its maximum value at some specific value of V_E', depending on different β

values. After the frequency approximately reverses its direction, further increase of V_E' causes a decrease in the growth rate. Then, the mode is fully stabilized by a large enough V_E'. This tendency of the growth rate is similar to the results for electrostatic drift wave [10] and the conventional electron temperature gradient mode [12].

We finally discuss effect of non-adiabatic electron on toroidal SWITG modes. We employ the following coupled integration equations for ϕ and $A_{//}$:

$$\left(1+Z_i\tau_i+\frac{k_\perp^{\ 2}}{2}\frac{\Omega_e^{\ 2}}{\omega_p^{\ 2}}\right)\phi=\sum_{j=i,e}\int_{-\infty}^{\infty}\frac{dk'}{\sqrt{\pi}}\ \times[H_j^{\ 00}(k,k')\phi+H_j^{\ 01}(k,k')A_{//}], \qquad (5\text{-}2)$$

$$-\frac{k_\perp^{\ 2}}{2\beta_e}A_{//}=\sum_{J=i,e}\int_{-\infty}^{\infty}\frac{dk'}{\sqrt{\pi}}\times[H_j^{\ 01}(k,k')\phi+H_j^{\ 02}(k,k')A_{//}], \qquad (5\text{-}3)$$

where $\phi(k)$ and $A_{//}(k)$ are the extended Fourier components in ballooning space of $\phi(r)$ and $-v_{te}A(r)/c$, and $k(k')=k_\vartheta s\vartheta(\vartheta')$, $\tau_j=T_e/T_i$, $Z_j=|q_j|/e$, and $M_j=m_j/m_e$, and we have normalized the wave numbers, k_ϑ, k and k' to $\rho_e^{\ -1}$, and the frequency ω to ω_e. The derivations of Eqs. (5-2) and (5-3) and explicit expressions for $H_j^{\ 00}, H_j^{\ 01}, H_j^{\ 02}$ are given in [14] and [15] and other parameters included in (5-2) and (5-3) are the standard notations. We should also note that the non-adiabatic electron response is taken into account in the set of equations (5-2) and (5-3).

Coupled equations (5-2) and (5-3) are solved numerically with the gyrokinetic integral equation code HD7. Previous results based on the electron adiabatic model can be easily recovered from the integral equation where ions and electrons are assumed to be adiabatic. The normalized growth rate multiplied by $k_\vartheta\rho_i$ is shown in Fig.24. Three unstable branches are presented with and without non-adiabatic electron effects under consideration, respectively. As $k_\vartheta\rho_i$ increases, the growth rate shows double humps, namely, the first peak around $k_\vartheta\rho_i\le 1$ is the conventional ITG mode, and the second peak at larger $k_\vartheta\rho_i$ is the SWITG mode. The normalized growth rate multiplied by $k_\vartheta\rho_i$ is shown in Fig.24. Three unstable branches are presented with and without non-adiabatic electron effects under consideration, respectively. As $k_\vartheta\rho_i$ increases, the growth rate shows

double humps, namely, the first peak around $k_\vartheta \rho_i \le 1$ is the conventional ITG mode, and the second peak at larger $k_\vartheta \rho_i$ is the SWITG mode.

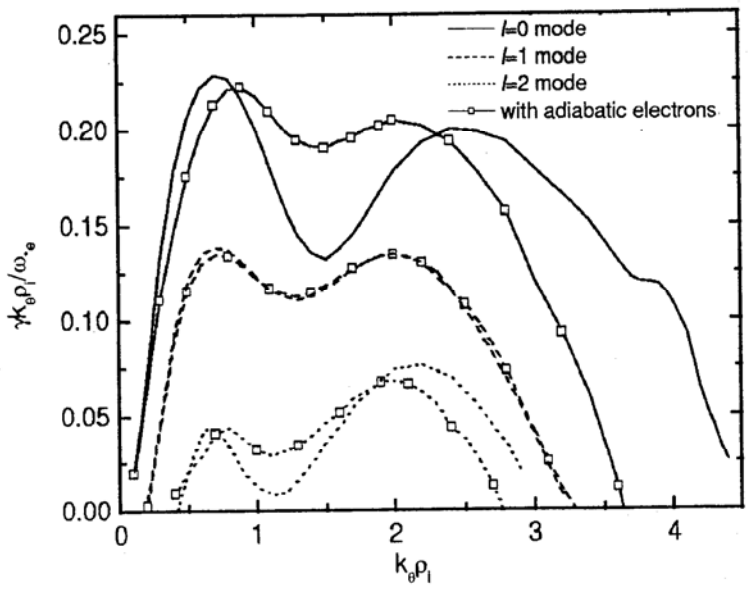

Fig. 25 Fig. 3 Normalized growth rate vs. $k_\vartheta \rho_i$ for $\eta_i = \eta_e = 2.5$, $\tau_i = M = Z_{eff} = 1$, $\hat{s} = 0.8$, $q = 1.5$, $\varepsilon_n = 0.1$ and $\beta_e = 0$. (from [27])

In Fig. 25, solid, dashed and dotted lines denote the different harmonic modes with l= 0, 1 and 2, respectively. The lines with squares are the corresponding results when electrons are assumed adiabatic. The unstable SWITG mode still exists even with adiabatic electron assumption. It turns out from this result that the ion contribution is essential for the SWITG mode especially at large $k_\vartheta \rho_i$. A series of SWITG modes are found in a sheared slab configuration, showing the double -humped behavior in the growth rate, which is similar to the result as shown in Fig. 3. So, it might be important to compare the similarity and difference between the toroidal SWITG and slab SWITG modes. It should be noted that the localization of the eigenmode in the ballooning space is strongly influenced by the nonadiabatic electron effect. In case of the adiabatic electron assumption, the eigenfunctions are rather smooth and localized

in ϑ space. When the non-adiabatic electron kinetics is taken into account, however, the eigenfunctions have broad structure along the magnetic field line and have oscillatory tails. This oscillatory structure in the tail leads to a large expenditure of computer time.

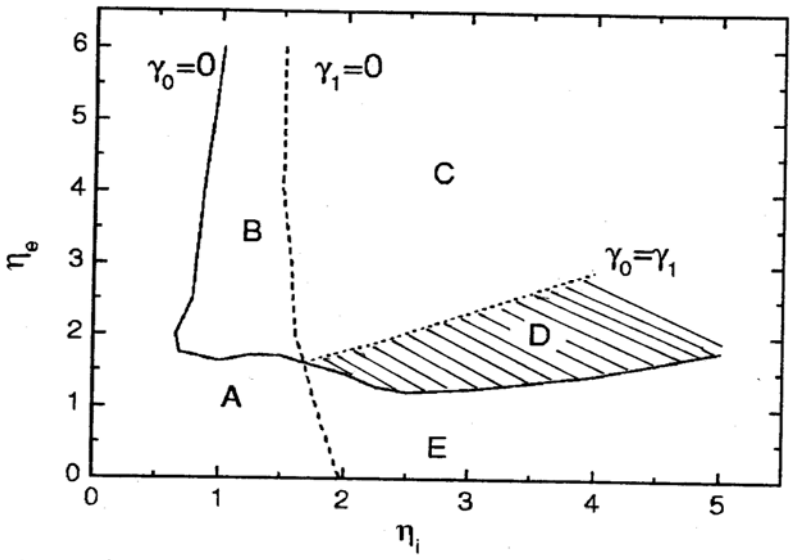

Fig.26 Stability diagram for l=0 and l=1 modes in $\eta_i-\eta_e$ space, where the solid and dashed curves denote the critical stability boundary of l=0 and l=1 modes. Parameters are the same as Fig.25. ([27])

Previous studies based on the adiabatic calculation indicates that the SWITG mode is unstable when both η_i and η_e exceed thresholds. When the nonadiabatic electron kinetics is considered, however, this conclusion is still valid for the fundamental mode (l=0) and not for the higher order modes. Temperature gradient dependence of the l=0 and l=1 modes for $k_\vartheta\rho_i=2$ is clearly shown in Fig.26. Three critical lines divide the $\eta_i-\eta_e$ diagram into five regions: both l=0 and l-1 modes are stable in the region "A", the l=0 mode is unstable in the region "B", "C", "D", and the l=1 mode is unstable in the regions "C", "D", and "E". So, the nonadiabatic electron kinetics strongly influences the l=0 mode. As the

result, in the region C and D, both l=0 and l=1 modes are unstable and in the region D (shown in Fig.4 by shaded region), where η_e is relatively smaller than η_i, the l=1 mode grows faster than the l=0 mode. Such situation has also been discussed in the bumpy torus plasmas [10].

5-5. Algebraic formula for critical gradient associated with anomalous transport

As mentioned in the introduction, understanding and controlling the anomalous transport experimentally observed are one of the key topics for magnetic confinement devices. There are strong evidence showing that an anomaly may be attributed to a various of small scale turbulences driven by gradients of plasma parameters such as density, temperature, velocity and so on. Particularly, the temperature gradient (TG) instabilities were the candidates responsible for the anomalous thermal transport. One of the most important achievements associated with this issue is identification of the ion temperature gradient (ITG) driven instability as the most plausible candidate responsible for the anomaly of ion thermal transport and the discovery of suppression effect of drift modes due to $E \times B$ sheared flow, which was discussed at the beginning of this Chapter. Recent experiments [48,49] show that ion thermal transport could be reduced to the neoclassical level with **ion internal transport barriers** (ITBs) but electron thermal transport hardly changes within ITBs, which was observed in the DIII-D tokamak [50]. On the other hand, **electron ITBs** were created in JET tokamak electron heating dominant discharges with $T_e/T_i \geq 3$ [51]. From these observations, electron temperature gradient (ETG) driven instability was also proposed as one of the driving mechanisms.

The correlation of the ETG turbulence and the electron thermal transport was studied theoretically with quasilinear theory in the 1980s. [52,53,54] The so-called electron temperature profile consistency (“stiffness” as termed recently) observed in experiments was successfully explained with the formula for electron conductivity discussed in these theory works.

Recently, the correlation of the ETG turbulence and electron thermal transport is actively studied by Dorland et al. [52], Jenko et al. [53.54], Watanabe, Sugama et al. [55] and Li et al. [56] with gyrokinetic nonlinear simulation. Also, the electron thermal transport was studied in detail in stellarator [57] and tokamak [58,59] experiments. These experiments showed that the thermal fluxes are offset linear functions of the temperature gradient (TG) parameter in regions close to the critical value of TGs. It turns out from these results that the critical observed experimentally are the threshold for the ETG driven instabilities from the turbulent transport point of view.

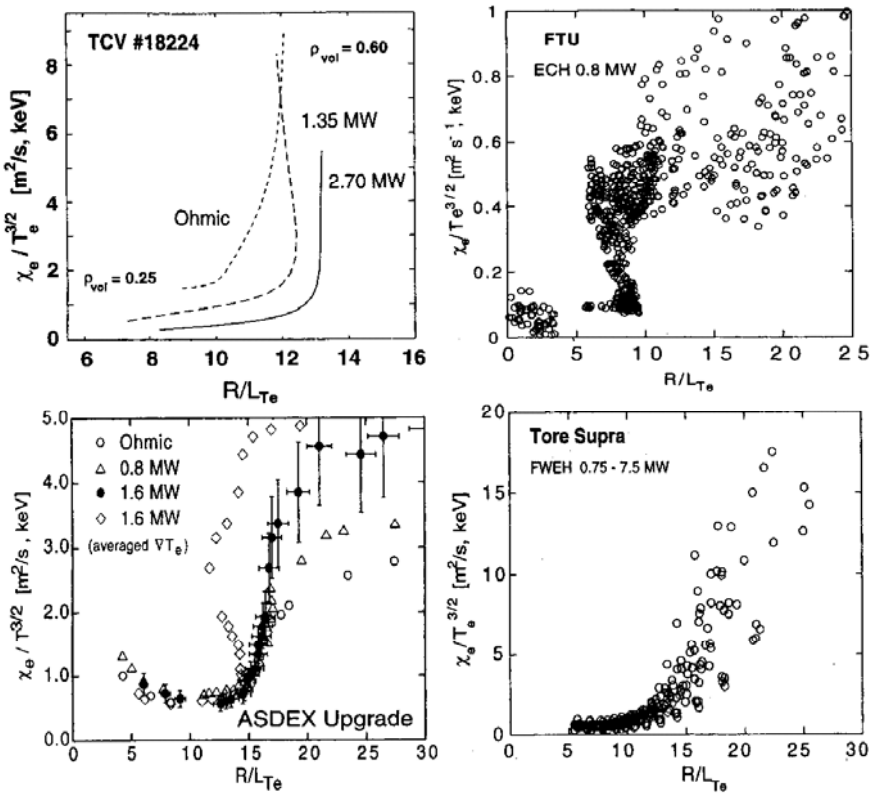

Fig. 27 Normalized heat diffusivity versus R/L_{T_e} for ASDEX Upgrade, FTU and TCV with ECH and Tore Supra with fast wave electron heating. ([59])

In specific studies of electron transport with dominant electron heating, the similar properties were found in typical tokamaks, namely, ASDEX Upgrade, RTP, FTU and TCV, where the heating method was ECH in L-mode plasmas. The wide range in size and wide range in density and magnetic field has been compared in Fig.27. (See, [59]) As was shown in this figure, despite these quite different experimental parameters, the T_e profile in these devices exhibit the almost constant value of $\nabla T_e/T_e$ in the confinement region and the values of R/L_{T_e} at mid -radius is quite comparable, between 8 and 12. All four machines clearly show a strong increase of electron transport above a threshold in R/L_{T_e}.

Gyrokinetic and gyrofluid simulations of ITG model and ETG instabilities and turbulence in tokamak plasmas as well as tokamak plasma thermal transport models have been studied to explain the experimental observations. Comparisons and physics basis of tokamak transport models have been shown in Fig.28. [60]

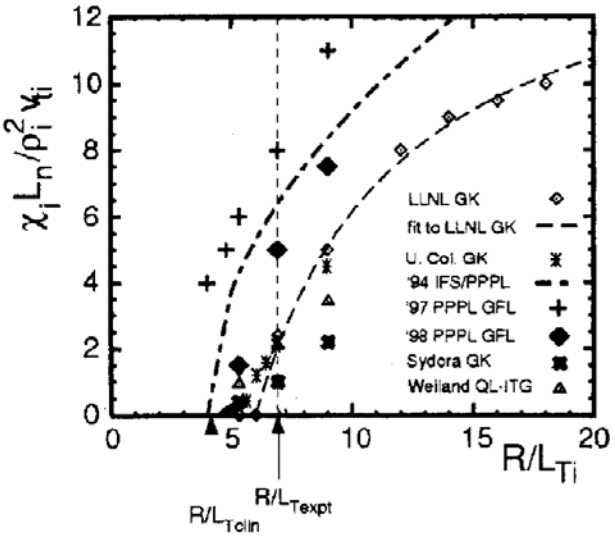

Fig.28 χ_i vs. R/L_T from the gyrofluid code using 1994, an improved 1998 gyrofluid closer, the 1994 IFS-PPPL model, the LLNL and U.Colorad flux-tube and UCLA (Sydora) global gyrokinetic codes, and the MMM model (Weiland QL-ITG) for the DIII-D Base case [60].

Figure28 shows predictions from the various simulations and models for χ_i vs. R/L_T for a scan about the DIII-D base case parameters. The agreement between two sets of flux-tube gyrokinetic results, namely, the U. Col. Boulder's results and the LLNL's results are very good although there is somehow difference at lower values of R/L_T. A remarkable good fit to LLNL gyrokinetic results is given by the following formula [60]

$$\chi_i L_n /(\rho_i^2 v_{ti}) \cong 15.4[1.0 - 6.0(L_T/R)], \qquad (5\text{-}4)$$

which is shown in Fig.28. This fit corresponds to an offset linear dependence of the thermal flux on the temperature gradient $Q \propto (R/L_T - R/L_{Teff.})$. The linear critical temperature gradient $R/L_{Tcrit.}$ has been checked by several different theories and codes. Detailed discussion is given in [60].

We here briefly introduce results for the ETG driven instability and turbulent transport in toroidal plasmas with gyrokinetic theory by J. Dong et al. [12,61]. The critical gradients, which may be compared with experimental observations, are accurately calculated without extrapolation. Estimations for the transport induced by the turbulence are also formulated with qusilinear theory (the mixing length theory). Particularly, the parameter dependence of the physics involved in the parameter regions close to the threshold of instability is emphasized in this study [61]. In order to study the maximum growth rate in the regime close to the instability threshold, we numerically solve the coupled integral dispersion equation for low beta plasmas, Eqs. (5-2) and (5-3). We finally get the following maximum growth rate and related electron thermal conductivity,

$$\gamma^{\max} \cong \frac{1}{0.0173\tau_i^2 + 1.95\tau_i + 1.18} \frac{ck_\vartheta{}^{\max} T_e}{eBR}\left[\frac{R}{L_{T_e}} - \left(\frac{R}{L_{T_e}}\right)^{ct}\right], \qquad (5\text{-}5)$$

$$\chi_e \approx \frac{D_B}{0.0173\tau_i^{\,2} + 1.95\tau_i + 1.18}\,\frac{c}{\omega_{pe}}\left[\frac{1}{L_{T_e}} - \left(\frac{1}{L_{T_e}}\right)^{ct}\right] \times F(\varepsilon_n, \hat{s}, q), \quad (5\text{-}6)$$

with abbreviation of

$$\left(\frac{R}{L_{T_e}}\right)^{ct} \equiv \begin{cases} 3.5 + 1.07\tau_i + 0.5\tau_i^{\,2}, & 0.5 \le \tau_i \le 1.5 \\ 2.35 + 2.59\tau_i, & 1.5 \le \tau_i \le 5.0 \end{cases}, \quad (5\text{-}7)$$

where $\tau_i = T_e/T_i$, $D_B = cT_e/eB$ being the diffusion coefficient defined by Bohm and $F(\varepsilon_n, \hat{s}, q)$ is an order unity function of the rest parameters, respectively. It is found that increasing the temperature ratio τ_i is in favor of suppression of the modes through both raising the critical TG and dropping the proportionality coefficient between the maximum growth rate and deviation of TG from the critical TG. This is in line with electron ITB formation experiment where an electron ITB seems easier to be realized in plasmas of $T_e/T_i \cong 3$[51]. Following the experimental observations [51], we discussed the stability criterion in this parameter space. The stabilization diagram of the $l=0$ and $l=1$ SWITG modes in $\eta_i - \eta_e$ space is shown in Fig. 29 for τ_i=1, 2, 3, where l indicates the harmonic order and $l=0$, $l=1$ modes are the fundamental even and odd modes, respectively.

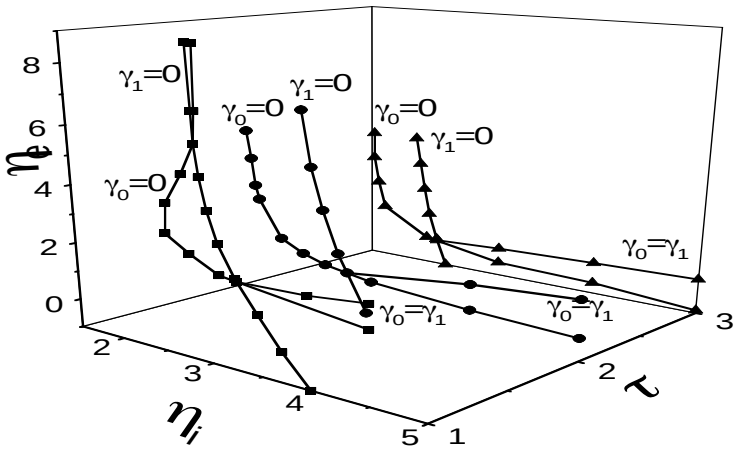

Fig. 30 Stabilization diagram for $l=0$ and $l=1$ modes in the $\eta_i - \eta_e$ space. Here, $\tau_i = T_e/T_i$ (=1, 2 and 3) is used. (From [62])

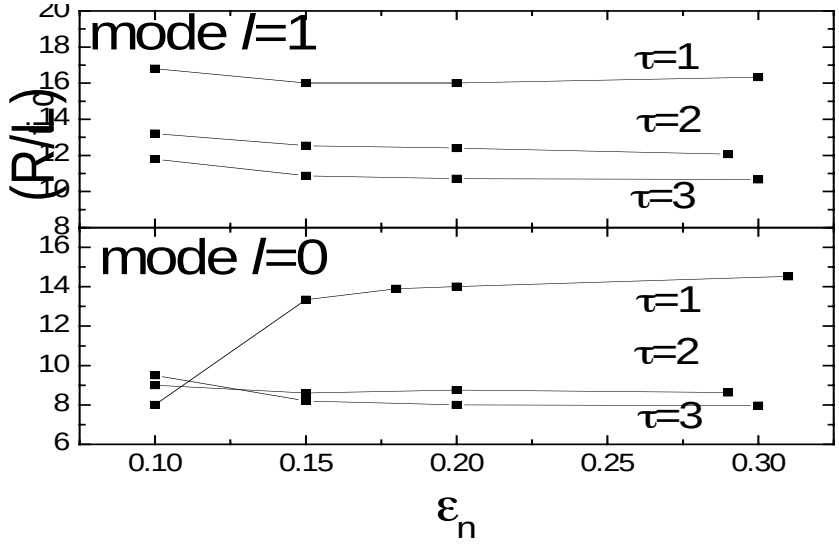

Fig. 31 Normalized critical ITG scale length $\left(R/L_{T_i}\right)_c$ versus $\varepsilon_n = L_n/R$, where L_n and R are the density gradient scale length and major radius, respectively (from [62]).

Marginal stability curves in ion/electron temperature gradient space $\eta_i - \eta_e$ are numerically obtained for the short wavelength ion temperature gradient (SWITG) instability as well as the scaling of the critical gradient with respect to temperature ratio, toroidicity, magnetic shear and safety factor [62]. In Figs. 30 and 31, these results are briefly shown. These results agree qualitatively with the experimental observations. Following theoretical predictions and experimental observations, experiments on DIII-D have been performed with the purpose of searching for evidence of a critical electron gradient or gradient scale length. Experiments employed off-axis EC heating to vary the local value of $\nabla T_e/T_e$. The following heat pulse diffusivity model [63]

$$H_e^{HP} \equiv \partial(\chi_e \nabla T_e)/\partial \nabla T_e = \chi_0 + f(T_e)[2(\nabla T_e/T_e) - k_{crit}]H_k, \qquad (5\text{-}8)$$

is proposed. This model undergoes a discontinuous increase when the local inverse gradient scale length, exceeds a critical value, k_{crit}, and the

Heaviside function H_k becomes nonzero. This jump in χ^{HP} produces a nonlinear change in T_e as k_{crit} is exceeded. Possible dependencies of $\chi^{HP}/T_e^{3/2}$ on $\nabla T_e/T_e$ are shown in Fig.32 along with a critical gradient dependence.

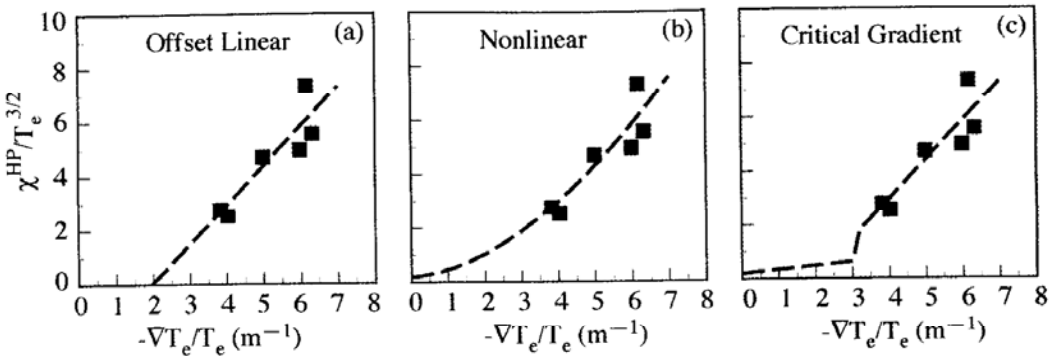

Fig.32 Dependences of normalized heat pulse diffusivity on inverse temperature gradient scale length allowed by the experimental results include (a) an offset linear dependence, (b) a nonlinear dependence and (c) a critical gradient dependence described by the model (5-8)(from [63]).

It turns out that no clear evidence of an inverse critical scale length was observed in this DIII-D experiment but the existence of the critical scaling cannot be ruled out by the experimental observations. More improved theory modeling and experiment are needed for close comparison between theory predictions and experimental observations.

Thermal transport barriers with high central electron temperature were established in the core of electron cyclotron heated plasmas on the Compact Helical System (CHS) experiment [57]. This was the first observation of an ITB for electrons (so-called electron ITB) on helical toroidal device, showing that the barriers were formed in the region where the density fluctuations associated with low frequency modes such as ITG

or ETG modes, reduced and the potential of the electric field changed drastically.

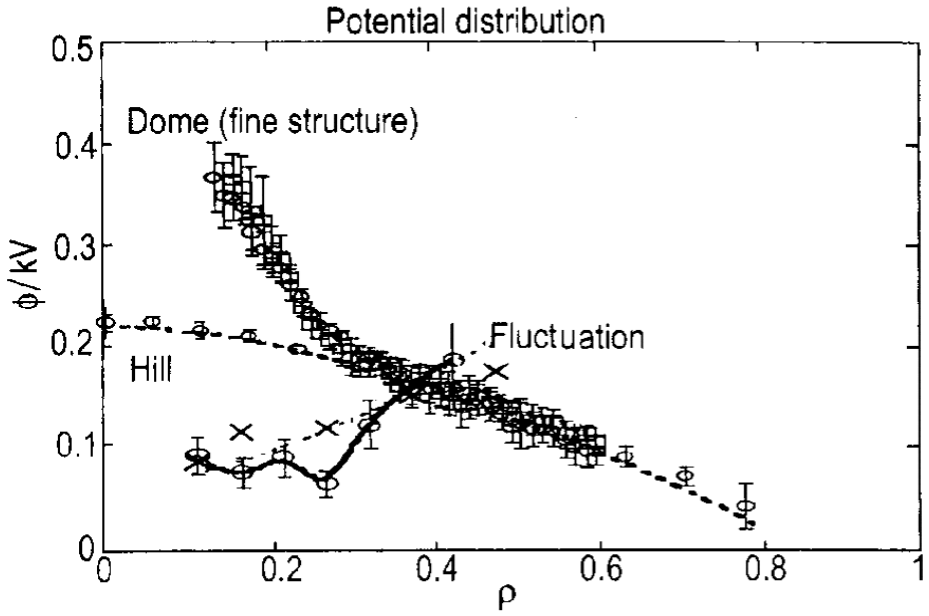

Fig. 33 Integrated fluctuation power as a function of radius together with potential profiles for the "hill" and the "dome" type radial profiles. (from [57] or [61]).

Plotted in Fig. 33 is the integrated fluctuation power as a function of radius together with the radial profiles of potential for the hill and dome type profiles. The reduction of fluctuation power at the shear maximum point is about 48% if the integral fluctuation level subtracted by the noise is used for the estimation. Figure 33 shows that an integral transport barrier (ITB) may be created at the suppression of turbulence. A unified formula for the L-mode and the H-mode associated with anomalous transport coefficient in the presence of inhomogeneous radial electric field is proposed base on self-sustaining interchange mode turbulence [64]. The thermal transport coefficient is given as

$$\hat{\chi} = \left(\frac{\hat{\chi}_L}{1 + G\hat{\omega}_E{}^2} \right), \qquad (5\text{-}9)$$

where $\hat{\chi}_L$ is the anomalous transport based on the L-mode plasma, $\hat{\omega}_E = \tau_{Ap}(mdE_r/dr)(rB)^{-1}$ where $\tau_{AP} = a/v_{Ap}$ (v_{Ap} is the poloidal Alfven velocity), and G is the geometric factor associated with equilibrium parameters such as the magnetic shear parameter s and β' whose explicit form is given in [64]. The suppression of transport caused by the $E \times B$ shear flow is prominent, provided that the shear flow is large enough. This reduction of the thermal transport and related scaling (5-9) has also been confirmed by the TEXTOR biasing experiment by Weynants et al. [65].

Acknowledgements

First, the author is grateful to Prof. T. Watanabe for his kindly guide to the topic discussed in this lecture when I jointed the theory group of IPP, Nagoya University. The author also acknowledges Prof. M. Watanabe (Kinki University) for his discussions on the eigenvalue problem for electromagnetic modes based on integral equation in k-space. The author wishes to thank Prof. R. Littlejohn (Univ. of Berkeley), Dr. R. Ferraro (JPL of Cal. Tech.), the late Prof. B.D.Fried (UCLA) for their fruitful discussions and collaborations on the nonlocal stability analysis during my visiting UCLA group. I also thank the late Prof. A. Banos (UCLA) for his valuable guide to the steepest descent method. I would like to acknowledge valuable discussions with Prof. T. Nishimoto (Tokyo Inst. of Tech.) and Prof. T. Kawai (Kyoto Univ.) at the meeting associated with WKB method in Kyoto University is gratefully acknowledged.

Valuable discussions and collaborations with Prof. K.Itoh, Prof. J.Q. Dong, Dr. Zhe Gao and Prof. H. Sugama concerning the nonlocal analysis of ITG and ETG modes are greatly appreciated. Finally, the author is indebted to Mrs. Y. Kohmoto for her kindness during completion of this lecture note.

The present work is partially supported by the JSPS-CAS Core University Program on Plasma and Nusion and also by the Collaboration Program of NIFS (NIFS04KDAD002) and the Grant -in Aid for Scientific Research of MEXT (15360495).

Appendix

Appendix 1: One-dimensional WKB problem (in general)

We write the Schrödinger equation in the form

$$\varphi'' + k^2(x)\varphi = 0,\ k^2(x) = 2[E - V(x)], \qquad \text{(A1-1)}$$

where E is the energy and V (x) is the potential energy, respectively. We here consider the case that the potential slowly changes in space with the condition, $kl >> 1$, where l is a characteristic distance over which V (x) changes appreciably. If we put the potential in the form (eikonal form),

$$\varphi = A\exp(iS)\ , \qquad \text{(A1-2)}$$

where A and S are real functions of x. Substitution of (A1-2) into (A1-1) yields

$$A'' + 2iA'S' + iS''A - S'^2A + k^2A = 0. \qquad \text{(A1-3)}$$

From the real and imaginary parts of (A1-3), we obtain the following coupled equations between amplitude A and phase S as

$$\begin{aligned} A'' + S'^2A + k^2A &= 0 \\ S''A + 2A'S' &= 0 \end{aligned}. \qquad \text{(A1-4)}$$

From (the second equation of (A1-4), we get $A'/A = -S''/2S'$, which gives

$$A = \frac{a}{\sqrt{S}}, \qquad \text{(A1-5)}$$

where a is a constant. From (A1-4) and (A1-5), we also have the relation, $(S')^2 = k^2(1 + A''/(Ak^2))$. Since we consider the case with $kl >> 1$, as mentioned under (A1-1), we get approximately

$$(S')^2 \cong k^2\ , \qquad \text{(A1-6)}$$

because the second term is negligible small compared with the first term with $A''/(Ak^2) \approx 1/k^2l^2 << 1$. Finally we have the solution

$$\varphi(x)=\frac{a}{\sqrt{k(x)}}\exp[\pm i\int_{x_1}^{x}k(x')dx'], \qquad \text{(A1-7)}$$

provided K>0, namely E>V. In the case of E<V (x), the solution becomes exponentially increasing or decreasing one as

$$\varphi(x)=\frac{a}{\sqrt{|k(x)|}}\exp[\pm\int_{x_1}^{x}|k(x')|dx']. \qquad \text{(A1-8)}$$

These solutions (A1-7) and/or (A1-8) is the WKB solution same as (3-13).

Appendix 2: Quantization and energy level for Coulomb Potential

Here, we discuss the energy level and quantization conditions for two cases, $l=0$ and $l\neq 0$ in the Coulomb potential. The quantization condition for $l\neq 0$ case is given [Ref.21] as

$$\int_{r_{min}}^{r_{\max}}\sqrt{2(E_n+\frac{Z}{r}-\frac{(l+1/2)^2}{2r^2})}dr=\left(n_r+\frac{1}{2}\right)\pi, \qquad \text{(A2-1)}$$

where $r_{min}, r_{\max}$ are the quasiclassical turning points which are shown in Fig.A1-b) and n_r is the radial quantum number.

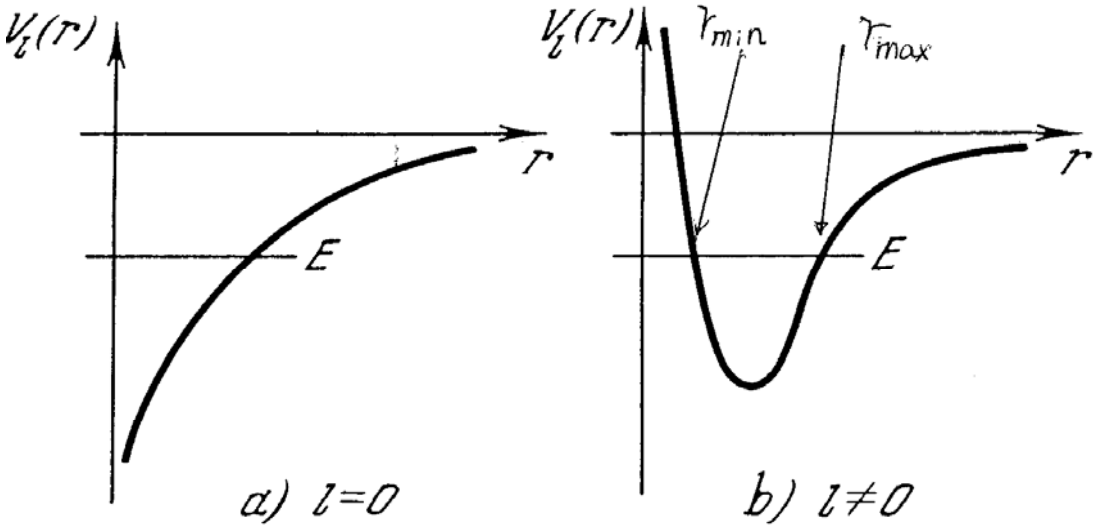

Fig.A1 Coulomb type potentials for two cases, a) $l=0$ and b) $l\neq 0$.

Since carrying out of the integration of the left hand side of (A2-1) yields $Z\pi/\sqrt{-2E_n}-(l+1/2)\pi$, we finally obtain the energy level, $E_n=-Z^2/(2n^2)$,

where $n = n_r + l + 1$ is the principal quantum number.

For large quantum numbers, the $l = 0$ wave functions in the Coulomb field, which is the spherically symmetric field, have the form (for $r << r_{\max}$) [Ref.27]

$$R_{n0} = a_1 Z^{3/2} \frac{J_1(\sqrt{8Zr})}{\sqrt{Zr}} \ , \qquad \text{(A2-2)}$$

where J_1 is the first order Bessel Function and a_1 is a normalization coefficient. Here, we note that when we consider quasi-classical motion in an spherically symmetric field, the angular variables ϑ, φ separate from the variable r and the wave function can be written as

$$\Psi_{nlm} = R_{nl}(r) Y_{lm}(\vartheta, \varphi), \qquad \text{(A2-3)}$$

where $R_{nl}(r)$ is the radial function and $Y_{lm}(\vartheta, \varphi)$ is the spherical harmonics. Using the expansions in series of Bessel function [Ref.26] for $rZ >> 1$ in (A2-2), we get approximately the following equation

$$R_{n0} \approx \frac{a_1 \cos(\sqrt{8Zr} - 3\pi/4)}{r^{3/4}}. \qquad \text{(A2-4)}$$

On the other hand, the quasi-classical solution for can be written as

$$R_{n0} = \frac{a_2 \cos(\int_0^r p_r dr - C_1 \pi)}{r\sqrt{p_r}} = \frac{a_2 \cos(\sqrt{8Zr} - C_1 \pi)}{r\sqrt{p_r}}. \qquad \text{(A2-5)}$$

Therefore, it turns out from (A2-4) and (A2-5) that the phase appearing in $R_{n0}(r)$ is $C_1 \pi = 3\pi/4$ instead of $\pi/4$ in the usual case. The function can be written in the following form

$$R_{n0} = \frac{a_3 \cos(\int_r^{r_{\max}} p_r dr - \pi/4)}{r\sqrt{p_r}}, \qquad \text{(A2-6)}$$

Where $r_{\max}$ is the right hand turning point. We finally obtain the condition that $R_{n0}(r)$ should be single valued, the quantization condition in the form

$$\int_0^{r_{\max}} p_r dr = (n_r + 1)\pi = n\pi. \qquad \text{(A2-7)}$$

Appendix 3: Physical meaning of the eikonal function g (k)

Substitution (4-11) into (4-3) gives the profile of wave amplitude $\phi(x)$ in the real space is given by

$$\phi(x) = \int dk \exp[-i\int_{k_0}^{k} g(k')dk' + ikx], \qquad \text{(A3-1)}$$

where we expressed the expression $\exp(ik_{\perp} + ik_{//} - i\omega t)$ for brevity. We carry out the integration with respect to k in (A3-1) by the method of steepest descents, which has been discussed in Sec. 4.3 of the Lecture Series- I and we obtain

$$\phi(x) \cong \sqrt{-2\pi i / g'(k_s)} \exp[-i\int_{k_0}^{k} g(k')dk' + ik_s x], \qquad \text{(A3-2)}$$

where k_s is the saddle point of the integrand in (A3-1), which is determined by $x - g(k_s) = 0$. Since the eikonal function $g = g(k)$ is determined by solving the integral equation (4-3), k_s is a function of x. If we transform the integration variable in (A2-2) from k' to $x'(\cong g(k'))$, (A3-2) reduces to

$$\begin{aligned}\phi(x) &\cong \sqrt{-2\pi i \frac{dk_s(x)}{dx}} \exp[-i\int_{x_o}^{x} x' \frac{dk'(x')}{dx'} dx' + ik_s x] \\ &= \sqrt{-2\pi i \frac{dk_s(x)}{dx}} \exp[i\int_{x_o}^{x} k'(x')dx' + ik'(x_0)x_0]. \qquad \text{(A3-3)}\end{aligned}$$

We note that (A3-3) is the WKB solution with wavenumber k at the point $x = g(k)$ because x_0 and $k'(x_0)$ are constants. The eikonal function in the k-space $g(k)$ represents the x-coordinate where the local wavenumber of the mode equals k.

Appendix 4 Multivalued Functions

Although the discussions of complex variables are often limited to single -valued functions, many theorems such as Cauchy's theorem must be reconsidered when we come to consider multivalued functions. Discussing a following example delineates the necessary concepts:

$$f(z) = z^{\frac{1}{2}}. \qquad \text{(A4-1)}$$

Let $z = re^{i\phi}, f(z) = \mathrm{Re}^{i\vartheta}$. Then we have the relations, $R = r^{1/2}, \vartheta = \phi/2$. This

function is multivalued. For a point on the z plane specified by (r, ϕ) or alternatively by $(r, \phi + 2\pi)$ two values of f (z) are obtained, namely,

$$f_1 = r^{1/2} e^{\frac{1}{2} i\phi}, f_2 = -r^{1/2} e^{\frac{1}{2} i\phi}. \qquad \text{(A4-2)}$$

The reason for the multiple values obtained here is the familiar fact that the square root of a number may have either a plus or a minus value. If the exponent were $1/4$ instead of $1/2$, there would be four possible values for f for a given z, namely,

$$(z^{\frac{1}{4}})_1 = r^{\frac{1}{4}} e^{\frac{1}{4} i\phi}, (z^{\frac{1}{4}})_2 = e^{\frac{1}{2}\pi i} (z^{\frac{1}{4}})_1, (z^{\frac{1}{4}})_3 = e^{\pi i} (z^{\frac{1}{4}})_1, (z^{\frac{1}{4}})_4 = e^{\frac{3}{2}\pi i} (z^{\frac{1}{4}})_1. \qquad \text{(A4-3)}$$

It should be noted that its phase may take on any value and this permits us in a calculation where the power of z is unspecified, to choose the phase of the function at will. This multiplicity of values introduces discontinuities into f. For example, at the point z=-r, $z^{\frac{1}{2}}$ has the value $ir^{1/2}$ if $z = re^{\pi i}$ or the value $-ir^{1/2}$ if $z = re^{-\pi i}$. Such discontinuities correspond to a representation of a barrier placed along the line $\phi = \pm\pi$. The mathematics of these problems involves multivalued functions.

Branch point, Branch lines, Branch cut and Riemann surfaces

The discontinuity in value may also be exhibited in a graphical manner by considering the conformal transformation generated by $z^{\frac{1}{2}}$. In Fig. (A2), we have drawn a circular contour $a \to b$ on the z-plane; its transform on the f=u+iv plane is a semicircle $A \to B$. Since circle $a \to b$ may have any radius, all the points on the z plane are correlated with only half of the points on the f plane where u>0.

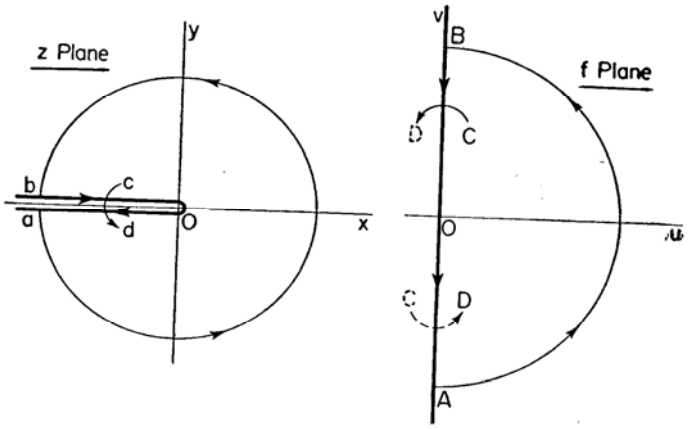

Fig. A2 Conformal transformation $f=\sqrt{z}$, showing multiple values and Branch line aob. (from Ref. [35]).

The values of f with u<0 will be correlated with those values of z whose argument lies between π and 3π. There are two values of f associated with each value of z. These values may be divided into two independent sets, those generated on the first tour of the x plane, $-\pi<\phi<\pi$ and those generated on the second tour $\pi<\phi<3\pi$. These two independent sets of values for $\sqrt{z}$ are called the **branches** of $\sqrt{z}$. The line, along which the discontinuities occur, $\phi=\pi$ is called the **branch lines**, which will be drawn as heavy double lines as shown in Fig. A2.

The particular reason for singling out the branch line is that, upon crossing the branch line in the x plane, such as for contour cd, we cross over from one branch of $\sqrt{z}$ to another, as we look at the transform of cd, the solid CD. This latter is drawn on the assumption that C is on the branch of $\sqrt{z}$ where u>0. If C were in the other branch, the image of cd would be the dashed CD. From the discussion of analytic continuation we know that there must be a singularity enclosed and z=0 is the singular point in this case. This type of singular point is called a **branch point**. The branch line runs from the branch point z=0 to the branch point at $z=\infty$, as shown in Fig. A2.

To establish single-valuedness and continuity for the purpose of applications of the various theorems, it is necessary to give separate

geometric meanings to the two-z plane regions. It is possible to do this process by using the notation of **Riemann surfaces**. For the function $\sqrt{z}$ under consideration, there are two Riemann sheets, namely the sheet 1 corresponding to $-\pi < \phi < \pi$, the sheet 2 corresponding to $\pi < \phi < 3\pi$. These sheets must be joined along the **branch cut**. As for the notations and definitions of the **Riemann Surface** and the **branch cut**, I would like to recommend an elegant book by **Morse and Feshbach** [Ref.35]. Although we can not discuss in detail about these topics in the present lecture, (see, Ref. [35]), how to cut each sheet along a branch line (called the branch cut), how to connect the lip of each side of the cut of a given sheet are briefly illustrated in Fig.A3 in the case of the function $f = \sqrt{z}$.

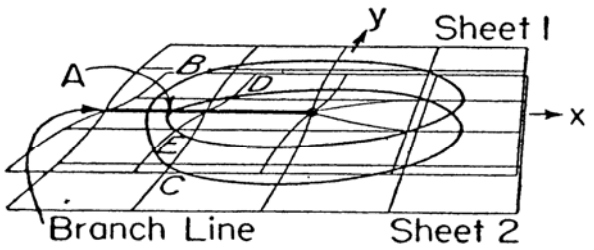

Fig.A3 Example of joining of Riemann surfaces along branch lines for the function $f = \sqrt{z}$. Here, the branch line is shown by heavy double line. (Ref. [35])

References (Lecture-2)

1) T. Watanabe, H. Sanuki and M.Watanabe, J. Phys. Soc. Jpn. **47**(1979) 286.
2) H. Sanuki, T. Watanabe and M. Watanabe: Phys. Fluids **23** (1980) 153.
3) P.J. Catto, R.E. Aamodt, M.N. Rosenbluth et al., Phys. Fluids **23**,764(1980).
4) L.R. Myra, P.J. Catto and R.E. Aamodt, Phys. Fluids **24**(1981)651.
5) R. Marchand, N.T. Gladd and Y.C. Lee, Phys. Fluids **25**(1982)338.
6) R. Linsker, Phys. Fluids 24(1981)1485.
7) R. Marchand, N.T. Gladd and Y.C. Lee, Phys. Fluids **25**(1982)338.
8) R. Marchand, C.F.Zhang and Y.C. Lee, Phys. Fluids **26**(1983)194.
9) N. Föman, Ann. Phys. (France) **61**,451(1970), N. Föman et al. Ann Phys. (France) **74**(1972) 314.
10) H. Sanuki, Phys. Fluids **27**(1984)2500.
11) R. D. Ferraro, H. Sanuki, R. G. Littlejohn and B. D. Fried: Phys Fluids **28** (1985) 2181, and also, R. D. Ferraro, R. G. Littlejohn, H. Sanuki and B. D.Fried: Phys Fluids, **30**(1987)1115.
12) Q. J. Dong, H. Sanuki and K. Itoh: Physics Plasmas **8**(2001)3635.
13) Zhe Gao, H. Sanuki, K. Itoh and J.Q. Dong, Phys. Plasmas **10**(2003)2831.
14) Zhe Gao, H. Sanuki, K. Itoh and J.Q. Dong, Phys. Plasmas **12**(2003)22502.
15) Zhe Gao, H. Sanuki, K. Itoh and J.Q. Dong, Phys. Plasmas **12**(2003)22503.
16) T.H. Stix, “The Theory of Plasma Waves”, McGraw-Hill Company, Chap.2.
17) M. Sato and Y. Terashima, (1969, October) JAERI-memo-3758.
18) B.D. Fried and S.D. Conte,” The Plasma Dispersion Function(Academic Press, Inc.New York,1961).
19) David L. Book, “NRL Plasma Formulary”, 1983 revised supported by The Office of Naval Research.
20) J.N. Davidson and T. Kammash, Nuclear Fusion **8**(1968)203.
21) ア・ベ・ミグダル、ヴェ・ペクライノフ著、“量子力学の近似的方法”ー物理現象へのアプローチー、岩崎与世夫訳、総合図書及び A.B. Migdal and V.P.Krainov, “Approximation methods in Quantum mechanisms”, W. A. Benjamin, Publishers Inc. New York, 1969. Chapter 3.
22) J. Heading, “ An Introduction to Phase Integration Method”, John Wiley&Sons, Inc.

23) Lecture Note by A. Banõs, Jr (UCLA, 1983), “Selected Topics on Asymptotic Methods”, (1983/12/15), private communications.
24) R. E. Langer, Phys. Rev. **51**(1937)669.
25) C.J. Hows, T. Kawai and Y. Takei, “Toward the Exact WKB Analysis of Differential Equations, Linear and Non-Linear”, Kyoto University Press (2000).
26) L.D. Landau and E.M. Lifshitz, “Quantum Mechnics” (Pergamon Press, London, 1959).
27) 岩波全書、岩波公式集 I, II, III （森口, 宇田, 一松 著）. Particularly, Vol. III, p154.
28) David Bohm, “Quantum Theory ”, Princeton-Hall, Inc., New York, U.S.A., (translated into Japanese) , ボーム著“量子論”、みすず書房、第３部１２章。
29) Leonard L. Schiff, “Quantum Mechanics “, McGraw-Hill Book Company, INC. (1955), (translated into Japanese), シッフ著、量子力学（井上健訳）吉岡書店、物理学叢書、上巻 ７章、pp.２１２~225.
30) A. Abramowitz and I. A. Stegun, “Handbook of Mathematical Function” (Dover), pp448-pp456.
31) H. L. Berk and D. Pfirsch: J. Math. Phys. **21** (1980) 2054.
32) T. Watanabe, M. Watanabe, H. Sanuki, K. Iino and K. Nishikawa, J. Phys. Soc. Jpn. **50** (1981) 1745.
33) H. Sanuki and R. D. Ferraro, Phys. Scr. **34** (1986) 54.
34) M. Watanabe, Y. Serizawa, H. Sanuki and T. Watanebe, J. Phys. Soc. Jpn. **50**(1981)1738.
35) P.M. Morse and H. Feshbach, “Methods of Theoretical Physics”, Mac Graw-Hill Book Company, New York, Part 1, Chapter4, pp398-pp403.
36) P.M. Morse and H. Feshbach, “Methods of Theoretical Physics”, Mac Graw-Hill Book Company, New York, Part 1, Chapter8, pp925-pp960.
37) Granino A. Korn and Theresa M. Korn,” Mathematical Handbook” for Science and engineers, McGraw-Hill book Company, Chapter15.3, pp492-.502.

38) R. Farengo, Y. C. Lee and P. N. Guzdar, Phys. Fluids **26** (1983) 3515.
39) J. Todoroki, Lecture note. (Private communication).
40) T. Watanabe, H. Hojo, M. Watanabe, H. Sanuki, T, Ohnuma and K. Nishikawa, 9th European Conf. on Controlled Fusion and Plasma Physics (Oxford, England, 1979) p57.
41) T.Ohnuma, T.Watanabe and H. Sanuki, Phs. Fluids **24** (1981) 2124.
42) T. Ohnuma, "Review on resonance cone field" IPP, Nagaya Univ. Res. Rep. IPPJ-446, pp1-78.
43) K. Miyamoto, "Plasma Physics for Nuclear Fusion", Cambridge Mass. MIT Press. Chapter12.
44) A. Mase et al., Phys. Rev. Lett. **64** (1990) 2281.
45) A. Boileau et al., Nucl. Fusion **32**(1992) 995.
46) A.I. Smolyakov, M. Yagi and Y. Kishimoto, Phys. Rev. Lett. **89** (2002) 125005.
47) H. Sanuki, Zhe Gao and J.Q. Dong, J. of Korean Physical Society, **49** (2006) S418.
48) C.M. Greenfield et al., Phys. Plasmas **4** (1997) 1596.
49) H. Shirai and JT-60 Team, Phys. Plasmas **5** (1998) 1712.
50) B.W. Stallard et al., Phys. Plasmas **6** (1999) 1978.
51) G.M.D. Hogeweij et al., Plasma Phys. Control. Fusion **44** (2002) 1155.
52) W. Dorland et al., Phys. Rev.Lett. **85** (2000) 5579.
53) F. Jenko et al., Phys. Plasmas **7** (2000) 1904.
54) F. Jenko et al., Phys. Plasmas **8** (2001) 4096.
55) T.Watanabe, H.Sugama, Y.Idomura, J.of Plasma and Fusion Research 81 No.7 (2005) pp534-pp546, No.8 (2005) pp581-pp592, and No.9 (2005) pp686-pp702 (in Japanese).
56) Li Jiquan et al., 21st IAEA Fusion Energy Conference, 16-21,October, 2006, Chengdu, China, TH/2-3.
57) A. Fujisawa et al., Phys. Plasmas **7** (2000) 4152.
58) F.Ryter et al., Phys. Rev. Lett. **86** (2001) 5493.
59) F.Ryter et al., Plasma Phys. Contl. Fusion **43** (2001) A323.
60) A.M. Dimits et al., Phys. Plasmas **7** (2000) 969.
61) L. Dong, G.Jian, A. Wang, H. Sanuki and K.Itoh, Nucl. Fusion **43** (2003) 1183.
62) Zhe Gao, H.Sanuki, K.Itoh and J.Q.Dong, J.Plasma Physics **72** (2006) 1249.

63) J.C.DeBoo et al., 20th IAEA Fusion Energy Conference, Vilamoura, Portugal, November 2004, IAEA-CN-116/EX/P6-13.

64) K. Itoh, S.I. Itoh, A. Fukuyama, H.Sanuki and M.Yagi, Plasma Phys. Contr. Fusion **36** (1994) 123.

65) R. Weynants et al., in H-mode workshop (1997).

66) Zhe Gao, J.Q.Dong and H.Sanuki, Phys. of Plasmas 11 (2004) 3053.